Geophysical Journal International

Geophys. J. Int. (2021) **225,** 2135–2156
Advance Access publication 2021 March 01
GJI Seismology

doi: 10.1093/gji/ggab085

Modelling the large earthquakes recurrence times along the North Aegean Trough Fault Zone (Greece) with a physics-based simulator

Christos Kourouklas [1], Rodolfo Console [2,3] Eleftheria Papadimitriou [1], Maura Murru[3] and Vassilios Karakostas[1]

[1] *Geophysics Department, School of Geology, Aristotle University of Thessaloniki, GR*54124 *Thessaloniki, Greece. E-mail: ckouroukl@geo.auth.gr*
[2] *Center of Integrated Geomorphology for the Mediterranean Area (CGIAM),* 85100 *Potenza, Italy*
[3] *Istituto Nazionale di Geofisica e Vulcanologia (INGV),* 00143 *Rome, Italy*

Accepted 2021 February 26. Received 2021 February 11; in original form 2019 December 4

SUMMARY

The recurrence time of large earthquakes above a predefined magnitude threshold on specific faults or fault segments is one of the key parameters for the development of long-term Earthquake Rupture Forecast models. Observational data of successive large earthquakes per fault segment are often limited and thus inadequate for the construction of robust statistical models. The physics-based earthquake simulators are a powerful tool to overcome recurrence data limitations by generating long earthquake records. A physics-based simulator, embodying well known physical processes, is applied in the North Aegean Trough (NAT) Fault Zone (Greece). The application of the simulation is implemented, after defining a five segment source model, aiming at the investigation of the recurrence behaviour of earthquakes with $M_w \geq 6.5$ and $M_w \geq 7.0$. The detailed examination of the 544 $M_w \geq 6.5$ earthquakes included in the simulated catalogue reveals that both single and multiple segmented ruptures can be realized along the NAT. Results of statistical analysis of the interevent times of $M_w \geq 6.5$ and $M_w \geq 7.0$ earthquakes per participating segment to the related ruptures indicate the better performance of the Brownian Passage Time renewal model in comparison to exponential model. These results provide evidence for quasi-periodic recurrence behaviour, agreeing with the elastic rebound theory, instead of Poissonian behaviour.

Key words: Numerical modelling; Earthquake interaction, forecasting and prediction; Seismicity and tectonics; Statistical seismology.

1 INTRODUCTION

The development of fault-based large earthquake recurrence models is an indispensable component of earthquake occurrence probability estimates for seismic hazard assessment. These models returns the likelihood of the occurrence of large earthquakes above a given magnitude threshold (e.g. $M \geq 6.5$) in a specified time span resulting in Earthquake Rupture Forecasts (ERF). The frequency–magnitude distribution (FMD) of earthquakes on specific fault segments is also a widely used approach to analyse the related seismic activity. A wide class of models are those studying the statistical behaviour of large earthquakes occurrences per fault segment. The key parameter of these models is the recurrence time of large earthquakes above a predefined magnitude threshold, associated with specific faults or fault segments in a study area. These earthquakes might be considered as characteristic earthquakes (Schwartz & Coppersmith 1984) in most of the cases. They get similar magnitudes near maximum for a given fault segment, are capable of rupturing the entire or most of the fault segment area, and have similar slip distributions. Either the memoryless Poisson model or a certain renewal one, that considers the occurrence times between consecutive earthquakes in the process, can be applied in the recurrence modelling. The latter model represents an elastic rebound motivated forecast (e.g. Rhoades *et al.* 2011 in New Zealand; Field 2015 in California; Valentini *et al.* 2019 in central Italy), in accordance with Reid's theory (Reid 1911) of seismic circle's stress built mechanism, which describes the ideal case of the large earthquakes temporal occurrence pattern of pure periodic behaviour.

The large earthquake recurrence times in specific fault zones are not regular but exhibit short- and long-term clustering (Kagan & Jackson 1991; Dieterich 1994). This is explained by physical processes, such as fault heterogeneity (Scholz 2002), occurrence of lower magnitude earthquakes that take up a part a sufficient amount of the accumulated strain and the interactions among fault segments due to the permanent and temporal stress changes (Stein *et al.* 1997; Hardebeck 2004). These are potential factors to influence the recurrence times by moving a fault towards or away from failure. This complexity implies that the recurrence time should be treated

with probabilistic models, rather than with deterministic ones (e.g. Mangira *et al.* 2019). The identification of as many as possible large earthquakes being associated with individual fault segments is required for a precise and robust modelling of the recurrence time applications along with the selection of the appropriate statistical model. These data set could include a variety of information coming from historical and instrumental earthquake catalogues and palaeoseismological observations.

Observational data are limited because of the long recurrence times of large earthquakes in a given fault segment and the shortage of earthquake catalogues. There are often available from 3 to 10 observations, resulting in large uncertainties on the recurrence parameter estimation (Ellsworth *et al.* 1999). Cases with recurrence times more than 10, above which the parameters estimates could be more robust, are rare. A special case in which the current known maximum number of a complete record of consecutive large earthquakes ($M_w \geq 8.0$) is reported is the Alpine Fault in New Zealand, containing 22 events (Berryman *et al.* 2012). This number is latter updated to 24 events by Biasi *et al.* (2015). Consequently, the probabilistic models are hard to be constrained and the discrimination among them is difficult. Specifically, a number of about 50 interevent time samples, as proposed by Matthwes *et al.* (2002), is required for robust selection among the candidate statistical models. The use of independent data sets such as palaeoseismic event dating (Biasi *et al.* 2002, 2015), slip per event constraints (Ogata 2002) and Bayesian methods (Nomura *et al.* 2011; Fitzenz 2018) are important additional alternatives in order to refine the parameter space of the models and also to compare their performance (Fitzenz & Nyst 2015).

The development of earthquake simulators is a powerful tool to overcome the aforementioned difficulties and limitations. Physics-based simulators applications could provide information about earthquake occurrence combining approximations of the known physics concerning stress transfer, frictional properties, fault geometry and kinematics. Starting from Rundle (1988), Robinson & Benites (1996) and Ward (2000), the concept of physics-based simulators has grown and several algorithms have been proposed (e.g. Richards-Dinger & Dieterich 2012; Sachs *et al.* 2012; Ward 2012; Schultz *et al.* 2017) and applied in California (Tullis 2012) and other regions worldwide such as New Zealand (Robinson *et al.* 2011; Christophersen *et al.* 2017). This concept has become popular over the years due to its ability to model and reproduce long earthquake occurrence records (e.g. lasting thousands or millions of years) with the final output of a simulated catalogue containing much more events than a real catalogue. These simulated catalogues attain many potential applications, in addition to the investigation of the earthquake recurrence behaviour, such as the study of the FMD on individual faults (Parsons *et al.* 2018), the calculation of short-term, time-dependent probabilities and testing and validation of scaling relationships as discussed in Field (2019).

Following this concept, Console *et al.* (2015) developed a physics-based simulator algorithm by modelling rupture growth and considering the long-term slip rates of the involved fault segments. This algorithm was firstly applied to simulate the seismic activity of the Corinth Gulf fault system in Greece, concluding in satisfactory results on the magnitude distribution of the simulated catalogue, adequately consistent with the observations and the realistic space time behaviour of the simulated seismicity (e.g. clustering of strong earthquakes and aftershock generation). Over the years, the simulation algorithm underwent an evolutionary improvement with the incorporation of additional parameters for the identification of successive ruptures (Console *et al.* 2017) and the inclusion of afterslip, treated by a decaying Omori-like power law (Console *et al.* 2018a). These improved versions were successfully applied to simulate the seismicity of Calabria (Console *et al.* 2017, 2018b) and the Central Apennines (Console *et al.* 2018a) in Italy. In both applications the simulated seismicity resembled the spatiotemporal features of the observed seismicity, including fault segments interactions and realistic and FMD, which are consistent with the observational catalogue.

In this study, a improved version of the simulation algorithm is applied, embodying in the physical processes the effect of the Rate and State Constitutive law proposed by Dieterich (1994), that contributes to the approximation of stress transfer and fault interaction at short timescales. This version has been already successfully applied in Central Italy (Console *et al.* 2020) and Central Ionian Islands in Greece (Mangira *et al.* 2020).

The major fault segments of North Aegean Trough Fault Zone (NATFZ) are modelled, for the investigation of their large earthquakes recurrence behaviour via the application and performance comparison of the Poisson model and the Brownian Passage Time (BPT) renewal model. NATFZ consists the dextral strike-slip active boundary between Eurasian Plate and Aegean microplate, moving at a relative motion of about 24 mm yr^{-1} (McClusky *et al.* 2000). Intense seismic activity is the result of this relatively fast motion, with frequent large earthquakes ($M_w \geq 6.5$) reported in both historical and instrumental catalogues. Their temporal occurrence pattern can be explained by triggering due to the stress transfer among the neighbouring major fault segments (Papadimitriou & Sykes 2001). These facts render the study area a particularly favourable and interesting case for applying a simulator algorithm and testing recurrence time models.

2 SEISMOTECTONIC SETTING AND DEFINITION OF FAULT MODEL

The driving mechanism of the active deformation in the Aegean region is the subduction of the oceanic lithosphere of Eastern Mediterranean under the continental Aegean microplate, forming the Hellenic Subduction Zone and the extensional back arc Aegean area (Fig. 1). The North Aegean Trough (NAT) (marked by the box in Fig. 1) consists the northern boundary of the Aegean microplate, first proposed by Papazachos *et al.* (1998) and further studied by many researchers (e.g. Kahveci *et al.* 2019). NAT is the westward prolongation of the North Anatolian Fault (NAF) into the Aegean Sea (Le Pichon *et al.* 1987; Armijo *et al.* 1999; Kreemer *et al.* 2004). Long-term slip rates vary from 22.5 mm yr^{-1} in the easternmost part of the NAT Fault Zone (NATFZ) to 4.9 mm yr^{-1} in the westernmost part, as derived from GPS measurements (McClusky *et al.* 2000; Floyd *et al.* 2010; Muller *et al.* 2013). This motion is mostly expressed by dextral strike slip faulting, which is supported by the available fault plane solutions (Fig. 2).

NATFZ is among the most active areas of the Aegean region with four large ($M_w \geq 6.5$) destructive earthquakes since 1970 occurring along neighbouring fault segments (Fig. 2). The activity of this period (1970–2020) encompasses enough instrumental earthquakes that allow an initial accurate quantitative analysis in terms of the estimation of the seismic parameters α and b, after the definition of the completeness magnitude, M_c. The FMD could provide an initial insight on the characteristic magnitude threshold from its deviations from the Gutenberg-Richter law in larger magnitudes. This latter issue must be confirmed by additional criteria, such as the expected

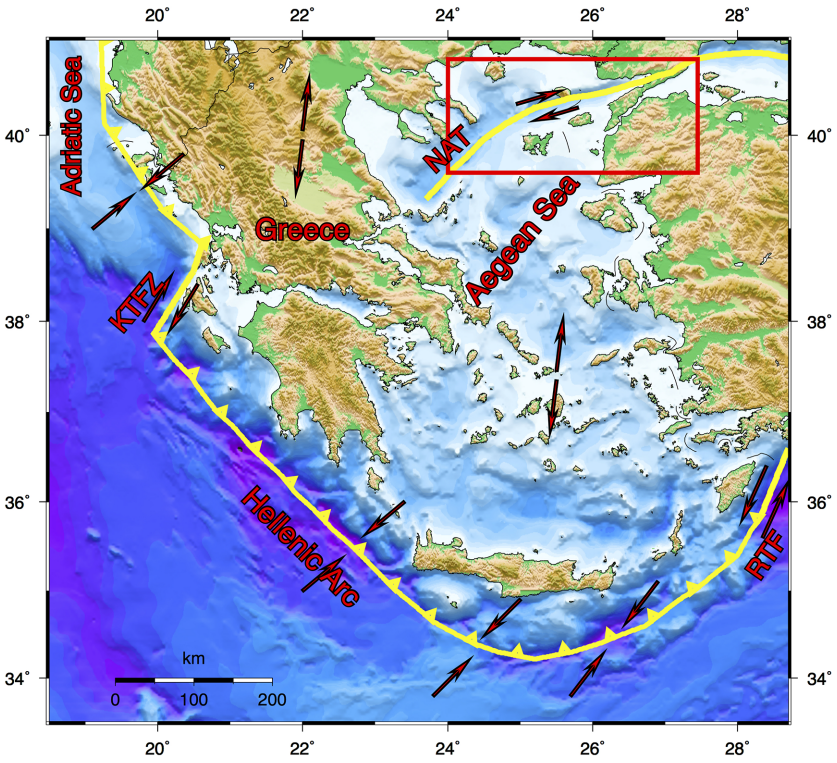

Figure 1. Main seismotectonic properties of the broader Aegean area along with the relative plate motions representing by the arrows, either side of the active boundaries depicted by the thick lines. The study area is denoted with a rectangular box.

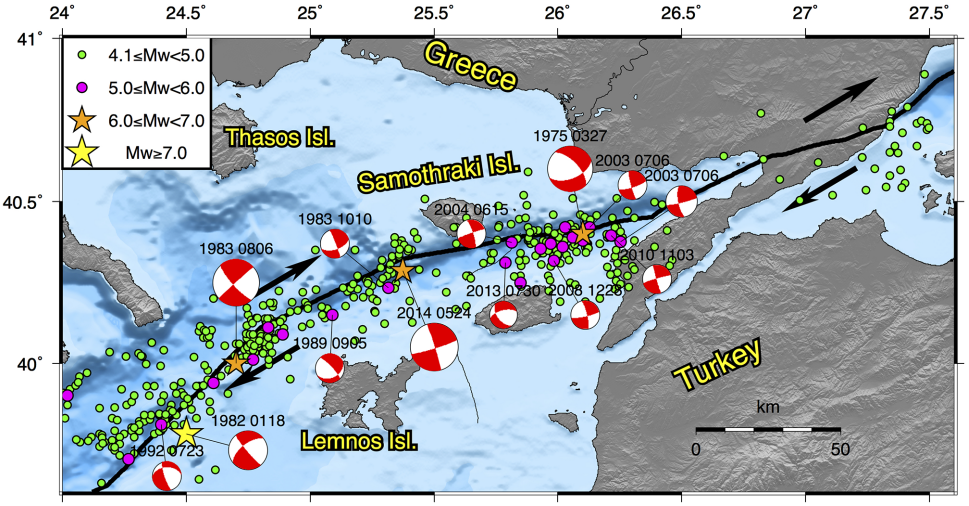

Figure 2. Seismicity of the North Aegean Trough Fault Zone (NATFZ; solid black line) since 1970. The small and moderate circles depict the $4.1 \leq M_w < 5.0$ and $5.0 \leq M_w < 6.0$ earthquakes, respectively. Moderate starts depict $6.0 \leq M_w < 7.0$ earthquakes, whereas the large star the $M_w \geq 7.0$ event. The available $M_w \geq 5.0$ fault plane solutions from Global Centroid Moment Tensor (GCMT; except for the 1975 $M_w = 6.6$ and the 1982 $M_w = 7.0$ earthquakes taken from Taymaz *et al.* (1991) and the 1983 $M_w = 6.8$ earthquake taken from Kiratzi *et al.* 1991) are plotted as equal area lower hemisphere projections. Parallel arrows represent the dextral strike-slip motion.

maximum magnitude (M_{max}) for each fault segment using scaling relations, for the definition of the characteristic magnitude.

The definition of M_c during 1970–2020 is investigated with the application of the Goodness of Fit method (GFT; Wiemer & Wyss 2000), considering the 90 per cent confidence level of residuals. The data used are taken from the regional catalogue of the Geophysics Department of the Aristotle University of Thessaloniki (1981; http:/geophysics.geo.auth.gr/ss) compiled with the recording of the Hellenic Unified Seismological Network (HUSN). The M_c is found to be equal to $M_c = 4.1$ (Fig. 3) and in agreement with Leptokaropoulos *et al.* (2012). The maximum likelihood estimate of b-value is equal to $b = 1.26$ and parameter α (annual) equals to $\alpha = 7.85$. These results show a deficit of moderate earthquakes ($4.8 \leq M_w \leq 5.1$ and $5.0 \leq M_w < 6.0$) and the absence of earthquakes ranging between $6.0 \leq M_w \leq 6.5$, which is an initial index of the magnitude threshold of large earthquakes occurrence in the study area, and later on this could support the selection of the characteristic earthquake magnitude.

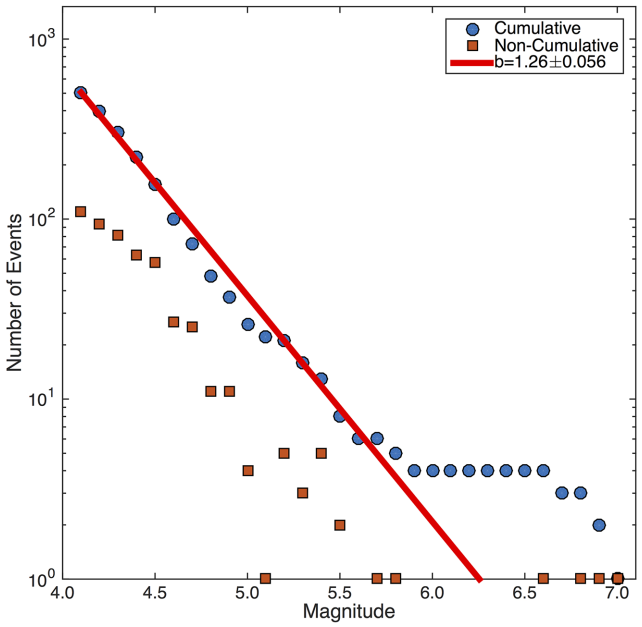

Figure 3. Incremental (squares) and cumulative (circles) number of the earthquakes versus magnitude (M_w) for the period 1970–2020. Straight red line represents the G-R law fit of frequency–magnitude distribution (FMD) using the the Goodness of Fit method.

Table 1. Focal parameters of the $M_w \geq 6.5$ large earthquakes occurred in North Aegean Trough Fault Zone (NATFZ) since 1845.

Date	Epicentral coordinates		M_w (σM_w)	Ref.
(yyyy-mm-dd)	Latitude	Longitude		
1859-08-21	40.30	26.00	6.9 (±0.3)	1
1864-06-14	40.30	25.00	7.3 (±0.3)	1
1887-05-14	40.10	25.20	7.0 (±0.3)	1
1893-02-09	40.49	25.53	6.8 (±0.3)	1,2
1905-11-08	40.00	24.50	7.5 (±0.3)	1
1912-08-08	40.62	26.88	7.4 (±0.3)	1,3
1912-09-13	40.10	26.20	6.7 (±0.3)	1
1975-03-27	40.40	26.10	6.6 (±0.2)	4,5
1982-01-18	39.78	25.50	7.0 (±0.2)	2,5
1983-08-06	40.00	24.70	6.8 (±0.2)	2,6
2014-05-24	40.28	25.37	6.9 (±0.2)	2,7

(1) Papazachos & Papazachou 2000; (2) Ambraseys 2002; (3) Aksoy *et al.* 2010; (4) geophysics.geo.auth.gr/ss; (5) Taymaz *et al.* 1991; (6) Kiratzi *et al.* 1991 and (7) globalcmt.org.

Information on the $M_w \geq 6.5$ earthquakes data, both instrumental and historical, is taken from the catalogue provided by Papazachos & Papazachou (2000) and the instrumental catalogue, comprising 25 large earthquakes since 1300 AD. The starting date since when the historical catalogue could be considered as complete, which is a crucial factor for recurrence modelling, is a still open question. Kourouklas *et al.* (2018) used two distinct data samples of $M_w \geq 6.5$ earthquake interevent times, the first starting in 1300 AD and the second one in 1600 AD, for investigating the recurrence pattern along the NATFZ fault segments. They found that the different assumptions for the starting date significantly affect the results related with the best performed recurrence models and the occurrence probabilities of future events. For this reason, in this study the complete $M_w \geq 6.5$ data sample starts in 1845 (following Papazachos & Papazachou 2000) and includes 11 earthquakes (Table 1) is adopted. The earthquake magnitudes of the historical catalogue, are expressed in equivalent moment magnitude scale based on relations proposed by Papazachos *et al.* (1997a) with an uncertainty equal to 0.3 ($\sigma M_{w\_hist} = \pm 0.3$), slightly larger than the magnitude estimation uncertainty in the instrumental period ($\sigma M_{w\_inst} = \pm 0.2$).

NATFZ continuously attracts the research interest and thus detailed geological, morphotectonic, geodetic, seismic reflection and precise seismological data are available. Combining all available information Kourouklas *et al.* (2018) proposed a model with five right-lateral adjacent strike slip fault segments onto which the stress is mainly accumulated and released, all of them associated with $M_w \geq 6.5$ earthquakes (Fig. 4). The westernmost termination of NAT, which is not associated with any known $M_w \geq 6.5$ earthquake, and exhibits a slip rate of 4.9 mm yr^{-1} (Muller *et al.* 2013), the lowest in the study area, is excluded from the analysis.

The proposed fault model for NATFZ consists of discrete and independent fault segments, without any overlapping. The current model is completely different than the UCERF3 (Field *et al.* 2014, 2015) relaxing segmentation approach, which is a mathematical discretization of major faults into subsections. The current approach is implemented by assuming the standard source characterizations of independent ruptured segments with fixed or multiple endpoints based on palaeoseismological data to show differences in rupture timing (Schwartz 2018). The major difference among the proposed model and the standard source characterization is that our study area is offshore and consequently palaeoseismological data or geological field survey results (e.g. Yang *et al.* 2020) are not available. However, the available information allows the definition of individual fault segments, based on structural and geometric criteria.

The first element of the current fault model definition is based on the precise swath bathymetry data and single channel seismic profiles provided by Papanikolaou *et al.* (2002) and Sakellariou *et al.* (2016). They have shown that two major basins, namely the North Aegean Basin to the west with a strike of its major axis equal to N42°E and the Saros Basin to the east with a relevant strike of N70°E, exist along NATFZ. These two wide basins are separated by a turning point northwest of the Lemnos Island (Fig. 4). Both the North Aegean and Saros basins can be later separated into two sub-basins, interpreting the swath bathymetry data seismic profiles of the aforementioned studies and seismic reflection data of Yaltirak & Alpar (2002) and McNeil *et al.* (2004). These findings evidence the potential existence of four fault segments, two in each major basin.

Advantageous for further identification of the four individual fault segments is the relatively recent occurrence of four large ($M_w \geq 6.5$) earthquakes (1975 $M_w = 6.6$, 1982 $M_w = 7.0$, 1983 $M_w = 6.8$ and 2014 $M_w = 6.9$). Their epicentres and focal mechanisms are in agreement with the formation and position of the sub-basins for both North Aegean and Saros basins.

Specifically, the 1982 $M_w = 7.0$ and 1983 $M_w = 6.8$ earthquakes are located in the southern margin of North Aegean basin, and their focal mechanisms (Taymaz *et al.* 1991 and Kiratzi *et al.* 1991, respectively) suggested a slightly change in strike, following the trend of the southern boundary of North Aegean basin. A sufficient fit among the dip direction (NW) shown by the fault plane solutions and the dip of the southern margin of North Aegean basin is also observed. Similarly, the 1975 $M_w = 6.6$ and 2014 $M_w = 6.9$ earthquakes occurred in the northern boundary of Saros basin and their focal planes as obtained from the respective focal mechanisms (Taymaz *et al.* 1991 and globalcmt.org, respectively) again follow the strike and dip changes of the corresponding sub-basins (Table 2).

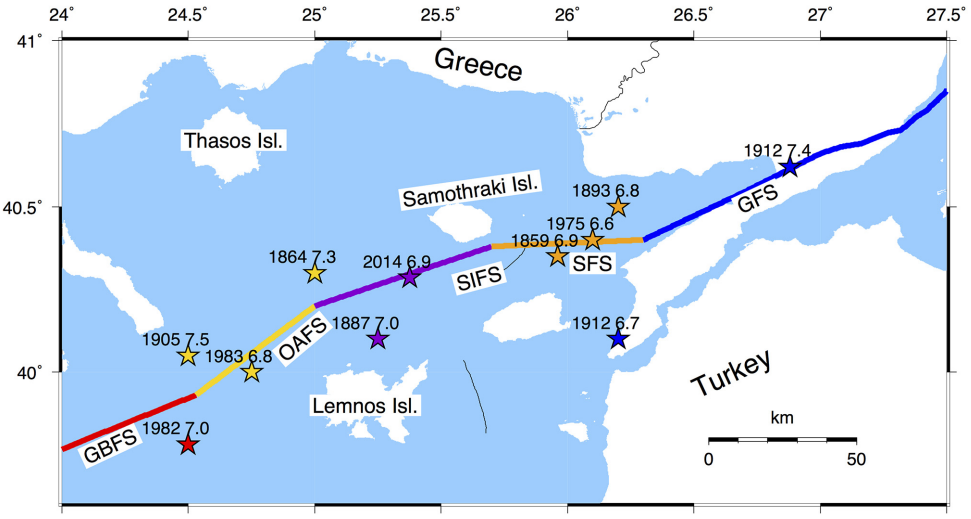

Figure 4. The fault segments model considered for the North Aegean Fault Zone. Thick lines represent each of the Glafki Bank (GBFS), offshore Athos (OAFS), Samothraki (SIFS), Saros (SFS) and Ganos (GFS) fault segments. Stars depict the $M_w \geq 6.5$ earthquakes since 1845 in association with their corresponding fault segment taken from Kourouklas *et al.* (2018).

Table 2. Parameters of the fault model for North Aegean Trough Fault Zone along with the maximum expected magnitude, M_{max}, obtained from scaling relations of Wells & Coppersmith (1994) and Papazachos *et al.* (2004) for strike slip faults. The thickness of the seismogenic layer is equal to 12 km for the entire the Fault Zone, with earthquake focal depths ranging between 3 and 15 km.

Fault segment code name	Upper left edge of segment		φ (°)	δ (°)	λ (°)	L (km)	W (km)	Slip rate (mm yr^{-1})		Maximum expected magnitude, M_{max}	
	Lat (°)	Lon (°)						Geodetic	Seismic	W&C[1] ($\pm1\sigma$)	Pap[2] ($\pm1\sigma$)
Glafki Bank	39.756	24.000	233	62	–173	48	14	12.5	7.5	7.0 (6.8,7.2)	6.7 (6.4,6.9)
Offshore Athos	39.390	24.530	228	89	–168	47	12	12.5	7.5	7.0 (6.8,7.2)	6.7 (6.4,6.9)
Samothraki	40.200	25.000	73	85	–177	60	14	21.2	13.0	7.1 (6.9,7.3)	6.9 (6.7,7.1)
Saros	40.380	25.700	68	55	–145	50	15	21.2	13.0	7.0 (6.8,7.2)	6.7 ($\pm1\sigma$)
Ganos	40.800	27.500	246	75	180	110	15	22.5	13.5	7.5 (7.3,7.7)	7.5 (7.3,7.7)

[1]Wells & Coppersmith (1994); [2]Papazachos *et al.* (2004).

In summary and starting from the west end of our study area, the Glafki bank and offshore Athos segments, exhibit NE–SW strike (233° and 228°, respectively), NW dip angles equal to 62° and 89°, respectively (Taymaz *et al.* 1991; Kiratzi *et al.* 1991) and extent about 48 and 47 km, respectively, in again agreement with the data provided by Papanikolaou *et al.* (2002, 2006). In the central part, the Samothraki and Saros fault segments are located, with an almost E–W strike and S–SE dip direction (Table 2; Taymaz *et al.* 1991; globalcmt.org) with lengths of about 60 and 50 km, respectively (Yaltirak & Alpar 2002; McNeil *et al.* 2004). These four fault segments constitute the main part of the NATFZ. The fifth segment of the NATFZ, namely the Ganos segment, is a well studied segment with a length of 110 km, a WSW–ENE strike and SE dip direction, being the western termination of the northern branch of North Anatolian Fault (Armijo *et al.* 1999, 2002; Ambraseys & Jackson 2000; Aksoy *et al.* 2010).

The fault segments are considered as rectangular planar finite sources. The thickness of the seismogenic layer is taken equal to 12 km, after considering accurately relocated earthquakes with focal depths ranging between 3 and 15 km (Hatzfeld *et al.* 1999, among others). The correspondence of each earthquake listed in Table 1 to specific fault segments by Kourouklas *et al.* (2018) is based on the analysis and revision of the available macroseismic data and damage reports contained in historical sources (Papazachos & Papazachos 2000; Ambraseys 2009).

It should be mentioned that a more simplified segmentation model was considered by Kourouklas *et al.* (2016) for studying the statistical properties of the $M_w \geq 6.5$ along NATFZ. Specifically, a three segment model with only two large segments composing the entire North Aegean and Saros basins, separated by the turning point northwest of the Lemnos Island (Fig. 4), and the individual Ganos fault segment. Their statistical analysis has shown earthquakes clustering in time. In contrast, the best performed model for the Ganos fault segment was the Inverse Gaussian one, which is an alternative formulation of the BPT model, implying quasi-periodic recurrence behaviour.

This clustering behaviour for both the North Aegean and Saros basins, as evidenced by the occurrence of large earthquakes close in space and time (e.g. the 1982 M_w= 7.0 and 1983 M_w= 6.8) is more likely to be explained by stress transfer among neighbouring fault segments rather than by different ruptured patches of a large enough single fault segment. This argument is also favoured from independent studies such as by Papadimitriou & Sykes (2001), who studied the evolution of stress in North Aegean Sea area. Summarizing, the advantage of the recent occurrence of large earthquakes along NAT in combination with high precision available structural data, along with the results of the early stage statistical analysis of the $M_w \geq 6.5$, synthesize the factors that led us to conclude in a five fault segments model.

The maximum expected magnitude, M_{max}, for each fault segment is calculated from the fault segments length via the application of the scaling relations of Wells & Coppersmith (1994) and Papazachos *et al.* (2004) for strike-slip faults, aiming at the examination of the consistency between the $M_w \geq 6.5$ earthquakes and their associated faults, assuming independent rupture segments. Maximum magnitude values estimated by the first relation are slightly higher than those derived from the second one, for the Glafki Bank, offshore Athos, Samothraki and Saros segments and exactly the same for Ganos segment (Table 2). The values obtained from Wells & Coppersmith (1994) relation are consistent with the observed magnitudes of the $M_w \geq 6.5$ earthquakes in all segments except for the historical $M_w \geq 7.0$ assigned to the offshore Athos segment, which likely corresponds to either multiple segment ruptures or possibly overestimated. These estimates support our fault model definition.

The amount of the strike-slip motion varies considerably from the easternmost to the westernmost segments of the NAT Fault Zone. Slip rates progressively decrease from 22.5 mm yr^{-1} in the eastern part (Ganos segment), to 21.2 mm yr^{-1} in the central part (Saros and Samothraki fault segments). The decrease is more dramatic in the western part of NATFZ (offshore Athos and Glafki Bank segments), where it decreases to 12.5 mm yr^{-1} (Muller *et al.* 2013). Jenny *et al.* (2004) compared the short- and long-term seismic moment rates with the long-term geodetic moment rates and concluded that the tectonic deformation of NATFZ is not fully coupled but involves an aseismic creep component. Specifically, their results showed that only 60 per cent of the geodetically determined tectonic deformation (average value of the ratio of the observed seismic and tectonic moment rates) is translated into seismic activity along the NATFZ. All the aforementioned data and parameters are taken into account in the construction of our fault model, which is the core input of the simulation procedure, and are summarized in Table 2.

3 SIMULATION PROCEDURE

The simulation algorithm was introduced and continuously developed by Console *et al.* (2015, 2017, 2018a, 2020). In this section, a brief outline is presented, including the main features along with the improvement of the current version. The simulator algorithm comprises several physical constraints, as the geometry and the long-term slip rates of each segment of the 3-D fault model, which achieve a self-organized magnitude distribution. Each fault segment is modelled as a rectangular planar source, onto which a normal grid of square cells is superimposed. The slip rate is distributed uniformly through the cells and could vary from one segment to the other. Each cell is initially assigned with a stress value arising from a random distribution, which then increases with time due to the continuous tectonic loading in terms of a backslip model. In a previous version of the simulator code, a rupture could start when the stress reached a value that exceeded the strength of a specific cell and then to expand to the neighbouring cells in a dynamic process. It is clarified that the simulation approach is only associated with the seismic part of deformation, without considering possible aseismic creep rate. Additionally, possible not fully coupled regions (coupling coefficient values less than the unity) could be considered by reducing the geodetic slip rate values that were initially assigned to the modelled fault segments, after taking into account the coupling ratio.

The main improvement of the present version of simulator is the inclusion of a new earthquake nucleation component, leading to a probabilistic mode of nucleation (Console *et al.* 2020). This is achieved by the contribution of the Rate and State Constitutive Law (Dieterich 1994), which operates a step before the nucleation process and controls the nucleation time of an earthquake. The seismicity rate, R, in each cell is calculated by:

$$R = \frac{r}{\left[\exp\left(-\frac{\Delta CFF}{A\sigma}\right) - 1\right]\exp\left(-\frac{\Delta t}{\gamma_0 A\sigma}\right) + 1}, \quad (1)$$

where r is the reference seismicity nucleation rate of each cell (defined as the seismicity rate R when $\Delta CFF = 0$), ΔCFF is the Coulomb Stress Change due to the coseismic slip of previous earthquakes, σ is the constitutive parameter expressing the response of the friction to a stress step change in a slip change (Toda & Stein 2003), where is a dimensionless fault constitutive parameter and σ the normal stress (Toda *et al.* 1998), Δt is the time elapsed since the stress change on a given cell and γ_0 is the inverse of the reference tectonic stressing rate, $\dot{\tau}_r$, ($\gamma_0 = \frac{1}{\dot{\tau}_r}$). The reference seismicity rate adopted in the simulation, is obtained by dividing the slip rate of each fault segment in the model by the slip pertaining to an event of average magnitude, assuming a GR magnitude distribution with $b = 1$, for events with magnitude exceeding the adopted threshold. Coulomb Stress Changes are computed by the equation:

$$\Delta CFF = \Delta\tau + \mu'\Delta\sigma_n, \quad (2)$$

where $\Delta\tau$ is the shear stress change in the slip direction, $\Delta\sigma_n$ is the normal stress change, positive for extension normal to the observational fault plane and μ' is the apparent coefficient of friction (Rice 1992).

Setting an initial value of Δt in equation (1) the expected number N of earthquakes in this time interval is estimated for all cells from the occurrence rate of equation (1). The probability of at least one event occurring in the Δt is given by $1 - \exp(-N)$, based on a Poisson distribution. If at least one cell exists where this probability exceeds a random number between 0 and 1, then the nucleation starts. If this is not the case, the probability is again computed for an increased value of Δt, and continues until a nucleation is implemented.

When nucleation begins, the strength of neighbouring cells is reduced according to a constant value multiplied by the square root of the number of the initially ruptured cells, resembling a weakening mechanism and promoting the growth of the rupture. The length expansion of each rupture is limited by a given number of times the width of the fault segment, prohibiting the rupture propagation in long distances. Rupture growth and termination are controlled by the inclusion of two free parameters in the algorithm, namely the strength reduction (S–R) coefficient, which refers to the fault weakening and the aspect ratio (A–R), which discourages the rupture propagation over long distances, operating in similar way as the dynamic triggering factor applied by Yikilmaz *et al.* (2010).

During the coseismic stage of the process, the stress decreases by a constant stress drop, Δp, value (e.g. $\Delta p = 3$ MPa) in every cell that participates in the rupture, whereas in the surrounding cells the stress changes according to the ΔCFF (Eq. 2) calculated onto each cell. A given cell can rupture more than once in the same earthquake. This happens when a cell in the initial stage of a large earthquake ruptures with a constant stress drop but not with a large amount of slip. Then, as the rupture grows, the neighbouring ruptured cells transfer positive Coulomb stress changes to the initially ruptured cells, recharging and reenforcing them to exceed the strength threshold once again, because this latter strength was decreased as the rupture area expands.

A rupture terminates when inside the activated area there are no more cells with stress exceeding their strength. Coulomb stress changes also contribute to the interactions among the causative and receiving segments, allowing the rupture expansion to neighbouring fault segments, which are located within a distance limit (e.g. 5 km). This feature of the algorithm represents the ability of fault interactions to possibly produce fault linkage and coalescence phenomena resulting in large earthquakes due to the simultaneous rupture of more than one segments (Scholz 2002).

4 APPLICATION OF THE SIMULATOR

The application considered each fault segment as rectangular planar source, consisting of 0.75 × 0.75 km square cells, with their parameters shown in Table 2. The minimum magnitude generated by the simulator is selected equal to 4.0 ($M_w = 4.0$), which corresponds to a two cells rupture. The values of rigidity, μ, and stress drop, Δp, are taken equal to 30 GPa and 3 MPa, respectively. Since the simulator considers the seismic part of deformation, the 60 per cent of the geodetically estimated slip rate is assumed to release coseismically, as derived from the average estimates of the coupling ratio for the study area calculated by Jenny *et al.* (2004). This percentage is also in agreement with Davis *et al.* (1997) who suggested this value for the Greek territory. Additionally, the historical event-based annual slip rate for the study area computed by Bulut *et al.* (2008), equal to 13 mm yr^{-1}, again agrees with the 60 per cent seismic contribution in the total slip rate. It is worth to mention here that additional applications of the simulation approach were tried by increasing the seismic part of the geodetically measured slip rate up to the 80 and 100 per cent, for the sake of comparison. The results evidence significant differences between the simulated and the observed occurrence rates of earthquakes with $M_w \geq 6.5$, a result that supports our choice. In summary, the used percentage of the geodetic slip rate, according to the values of coupling ratio calculated by Jenny *et al.* (2004), harmonizes the locked area percentage with the slip rate percentage, like an integration of the fault patches over the entire fault area. The simulation results that detect cells with higher stress budget than their neighbouring ones, provides a kind of such approximation.

The product $A\sigma$ of the Rate and State law, the *S*–*R* coefficient and the *A*–*R*, which are the three free parameters of the algorithm, must be specified before the simulation application. A wide range of $A\sigma$ values are proposed in previous studies. Harris (1998) and Harris & Simpson (1998) reported values ranging from 0.0012 to 0.6 MPa, as obtained from different earthquake sequences. Leptokaropoulos *et al.* (2012) studied the seismicity rate changes in the North Aegean Sea area using values of $A\sigma$ ranging between 0.0125 and 0.05 MPa, and especially, for the NATFZ between 0.04 and 0.05 MPa. Since the value of the product $A\sigma$ is not fixed, a range from 0.04 to 0.07 MPa with a step of 0.01 MPa was tested in this study ($A\sigma$ = [0.04 MPa–0.07 MPa]).

The fault weakening mechanism is rather uncertain, because the relevant knowledge is based not on straight forward observations (e.g. past seismicity). Since it is a crucial factor of the simulator procedure, a range of *S*–*R* values are also tested in the simulation, starting from a value equal to 0.1, which represents strong faults, and with a step of 0.1 up to the value of 0.4, which implies enhanced weakening (*S*–*R* = [0.1–0.4]). The value of the third parameter, *A*–*R*, is assigned after testing values equal to 7 and 10. These values denote rather elongated seismogenic sources, concordant for almost pure strike slip faults (*A*–*R* = [7 and 10]). Summarizing, the combination of the values of the three parameters was tested in the simulator application multiple times. Specifically, 32 different combinations stemmed from the above-mentioned parameters values ranges (Table 3), with the duration of each simulation equal to 10 kyr and a warm up period of 2 kyr.

Table 3. Values of the input parameters (σ, *S*–*R* and *A*–*R*) for each simulated catalogue and the corresponding *p*-values of the two sample Kolmogorov–Smirnov (KS2) and Wilcoxon Rank–Sum (WR–S) tests at 0.05 level of significance ($\alpha = 0.05$) of the simulated versus observed annual occurrence rates.

Simulation #	σ (MPa)	*S*–*R*	*A*–*R*	*p*-Value	
				KS2	WR-S
01	0.04	0.1	7	0.709	0.622
02		0.2		0.693	0.444
03		0.3		0.898	0.699
04		0.4		0.989	0.994
05		0.1	10	0.760	0.819
06		0.2		0.760	0.762
07		0.3		0.936	0.982
08		0.4		0.936	0.701
09	0.05	0.1	7	0.639	0.444
10		0.2		0.693	0.490
11		0.3		0.898	0.622
12		0.4		0.936	0.784
13		0.1	10	0.686	0.453
14		0.2		0.693	0.559
15		0.3		0.7600	0.959
16		0.4		0.936	0.684
17	0.06	0.1	7	0.427	0.266
18		0.2		0.693	0.471
19		0.3		0.897	0.682
20		0.4		0.999	0.990
21		0.1	10	0.678	0.462
22		0.2		0.760	0.739
23		0.3		0.936	0.133
24		0.4		0.936	0.673
25	0.07	0.1	7	0.468	0.367
26		0.2		0.693	0.471
27		0.3		0.898	0.665
28		0.4		0.989	0.982
29		0.1	10	0.482	0.408
30		0.2		0.760	0.728
31		0.3		0.760	0.958
32		0.4		0.936	0.695

Each triplet of input parameters and upon the specific values, results in a simulated catalogue with different total number of events, occurrence rates and maximum magnitude. An example of the influence of each parameter is shown in Fig. 5. The tested values of the product σ (keeping constant the values of *S*–*R* and *A*–*R*) produce catalogues with almost equal total number of events and the same maximum magnitudes. The main effect of σ is related with the occurrence rate of large earthquakes. As the values increase, the occurrence rate of the larger earthquakes also increases (Fig. 5a). The influence of the other two free parameters, the *S*–*R* and *A*–*R*, was already analysed by Console *et al.* (2015, 2017, 2018a), and are also discussed in this study. The *S*–*R* coefficient mainly controls the ratio between the number of small to large events. As clearly shown in Fig. 5(b), the smallest tested value (*S*–*R* = 0.1; denoted by triangles in Fig. 5b) results in a simulated catalogue with a number of small to moderate earthquakes 10 times larger when compared with the catalogue in which the largest tested value (*S*–*R* = 0.4;

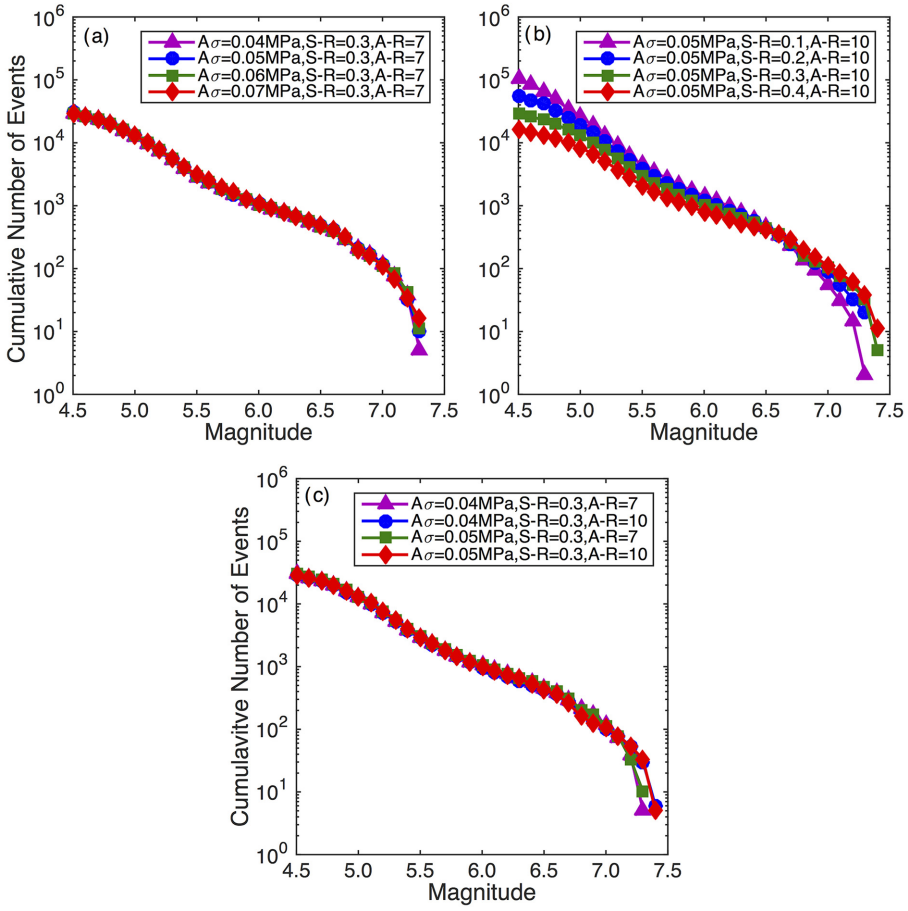

Figure 5. Examples of comparison between the frequency–magnitude distribution (FMD) of earthquakes obtained from simulated catalogues lasting 10 kyr, illustrating the influence of the different values of σ (constant *S–R* and *A–R*) (a), *S–R* (constant σ and *A–R*) (b) and *A–R* (constant σ and *S–R*) (c).

denoted with diamonds in Fig. 5b) are used. Complying with that, the number of large earthquakes exhibits the inverse proportionality. The smallest values of *S–R* produce simulated catalogues with ten times fewer large events than the largest *S–R* values. Consequently, the *b*-value of a given simulated catalogue is also controlled by this effect. For example, the maximum likelihood calculation (Aki 1965) of *b*-values of the catalogues produced with $S\text{–}R = 0.1$ and $S\text{–}R = 0.4$ are equal to 1.39 ($b_{S\text{-}R\,=\,0.1}$= 1.39) and 0.80 ($b_{S\text{-}R\,=\,0.4}$= 0.80), respectively.

The effect of the *A–R* value is mainly related with the maximum magnitude and neither with the total number of events nor with the *b*-value of the simulated catalogues. Since the larger the *A–R* value the larger the expansion of a rupture will be, the maximum magnitude of the catalogue is also larger. Comparing a pair of catalogues with constant values of σ and *S–R* and focusing on the influence of the two different tested values of *A–R* (e.g. either the triangles and circles or the squares and diamonds in Fig. 5c) a difference of 0.1 magnitude bin is reported for the maximum magnitude in each case ($M_{max} = 7.3$ for $A\text{–}R = 7$ and $M_{max} = 7.4$ for $A\text{–}R = 10$). In both cases of the *A–R* tested values, the maximum magnitude of the simulated catalogue differs from the observed one, which equals to 7.5 ($M_{max\_obs} = 7.5$). This difference may be attributed to the fact that the maximum observed magnitude refers to an earthquake of the early instrumental era, the 18 November of 1905 earthquake, whose magnitude might be possibly overestimated.

The assessment of the performance of each simulated catalogue was accomplished with comparison with observational data. The comparison is implemented via the application of the two sample Kolmogorov–Smirnov (KS2, Stephens 1974) and the Wilcoxon Rank–Sum (WR–S, Wilcoxon 1945; Mann & Whitney 1947) statistical tests at the significance level, α, of 0.05 ($\alpha = 0.05$; Appendix A1), between the cumulative annual occurrence rates of each simulated catalogue and an integrated observational catalogue contains both instrumental and historical earthquakes. The integrated complete catalogue contains events with $M_w \geq 4.5$ from 1970, $M_w \geq 5.0$ from 1950, $M_w \geq 5.2$ from 1911 and $M_w \geq 6.5$ from 1845, adopting the completeness thresholds that were suggested by Papazachos & Papazachou (2000). The cumulative earthquake number for each period (Fig. 6) shows that the selected magnitude ranges can be considered as complete for the $M_w \geq 4.5$, $M_w \geq 5.0$ and $M_w \geq 5.2$, for the respective periods, while the $M_w \geq 6.5$ earthquakes deviates from the G–R law, indicating the characteristic earthquake pattern, along with the limited number of $6.0 \leq M_w \leq 6.5$ earthquakes, for the period since 1845.

The integrated FMD (Fig. 7) is studied with the Milne & Davenport (1969) method of reduction of different completeness period data sets to a common time window. The estimation of parameters of α and *b* is implemented with a least square approach, which is commonly used in relevant cases (e.g. Papazachos *et al.* 1997b), and were found equal to $\alpha = 5.65 \pm 0.1$ (annual value) and $b = 0.730 \pm 0.03$. The least square estimate of the seismic parameters

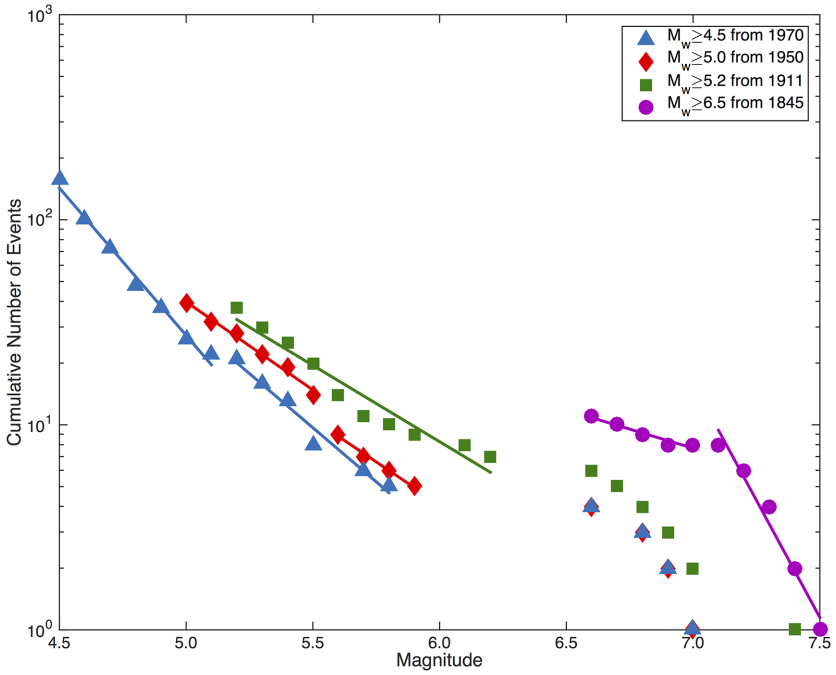

Figure 6. Frequency–magnitude distribution (FMD) of earthquakes occurred in NATFZ for four different periods. Straight lines indicate the magnitude range for which each catalogue considered as complete for the corresponding period.

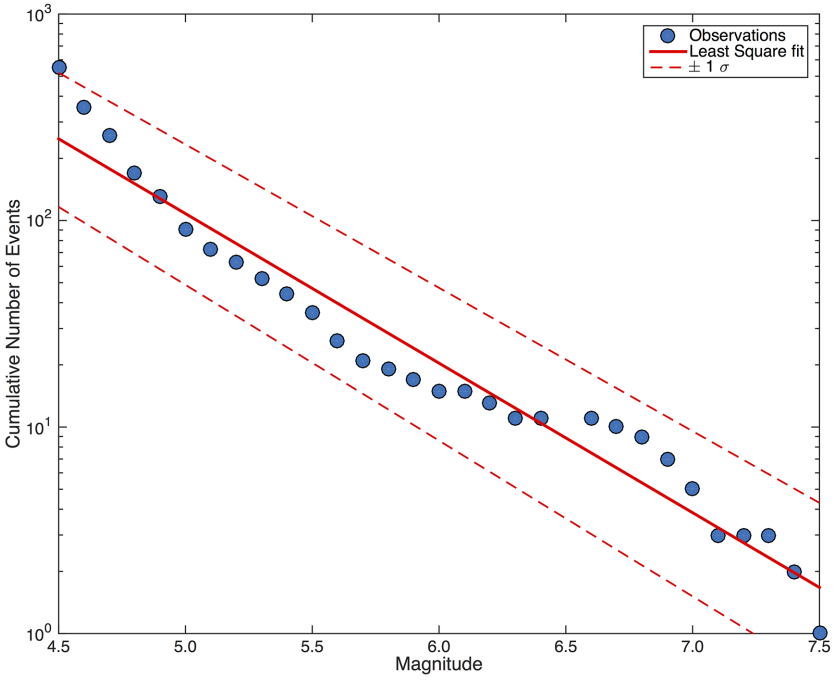

Figure 7. Frequency–magnitude distribution (FMD) of the integrated observational catalogue obtained with the data reduction method, along with its least squares fit of G–R law and the corresponding $\pm 1\sigma$ confidence bounds.

α and b is preferred, instead of the maximum likelihood method for different time windows proposed by Weichert (1980), because it provides more stable results.

Since the completeness magnitude of the integrated observational catalogue is selected equal to $M_c = 4.5$, the comparison of annual rates starts from this magnitude bin until the maximum magnitude found in each simulated catalogue, excluding the lower magnitude ($4.0 \leq M_w < 4.5$) simulated earthquakes. It is implemented by applying the tests to the cumulative number of events, N_i, for each magnitude bin divided by the corresponding period (N_i/period, in years), under the null hypothesis that the two rates come from the same population. The applied tests provoke such comparison because they are non-parametric (distribution free) and they do not use any estimated parameter from the samples under testing. On

the other hand, their results must be treated with caution of the sensitivity before the final decision will be taken.

The results of the two statistical tests are shown in Table 3 and Fig. 8 in terms of their corresponding *p*-values, from which it became clear that in all cases their values are quite larger than the significance level (0.05). More precisely, the *p*-values of the KS2 test range from 0.472 to 0.999, with 3 out of the 32 values being larger than 0.98 (p-value > 0.98), showing a good performance with respect to the observational data. These values are pertaining to the simulations 04, 20 and 28. Additionally, the ones computed from the WR–S test fluctuate between 0.133 and 0.994, with 4 picks of very large values (p-value > 0.98), corresponding to simulations 04, 07, 20 and 28. Combining these results, the best performed simulated catalogues based on the maximum *p*-values of both tests are the catalogues of the simulations 04, 20 and 28. From a statistical point of view, simulation 20 results in slightly higher *p*-values than the others. To overcome the sensitivity of these results, additional criteria must be applied for the final decision of the best performing catalogue. These criteria include the comparison among the *b*-values and the annual moment rate, of both the observational catalogue and the best performed ones. The *b*-value of the integrated observational catalogue is equal to $b = 0.73$, and for the simulations 04, 20 and 28 equals to 0.81, 0.78 and 0.79, respectively. The annual moment rate, $\dot{m}_o$, of the observational catalogue is equal to 1.91e+18 Nm yr^{-1} and those of the simulated catalogues 04, 20 and 28 equals to 1.51e+18, 1.54e+18 and 1.52e+18 Nm yr^{-1}, respectively. The latter results further confirm the statistical test results, since both the b and $\dot{m}_o$ values are the closest to the observed ones, supporting the simulated catalogue 20 (Fig. 9) as the best performing one. This catalogue will be used for the earthquake recurrence analysis.

The best performing simulated catalogue is the one produced with the parameter values of $\sigma = 0.06$ MPa, $S–R = 0.4$ and $A–R = 7$, comprising 32 143 events with $M_w \geq 4.0$ and 17 069 with $M_w \geq 4.5$ during the 10 kry of the simulation and with the largest magnitude equal to 7.3 ($M_{w\_max} = 7.3$). Fig. 9 shows the annual occurrence rates of the simulated catalogue, against the observed occurrence rates, where only some mismatches appear, mostly for events of $M_w > 6.3$. These discrepancies are basically caused by the fact that most of large events in the observational catalogue belong to the historical or the early instrumental period, when their magnitudes are possibly overestimated, increasing their occurrence rates and the maximum magnitude of the corresponding catalogue. In any case, the confidence bounds of the integrated observed annual occurrence rates allow us to accept that the simulated catalogue represents quite accurately the regional seismicity.

5 LARGE ($M_w \geq 6.5$) EARTHQUAKES OCCURRENCE AND RECURRENCE MODELLING

The main purpose of the simulation application is the study of the recurrence behaviour of large events in each one of the five segments of NATFZ, for which a couple of criteria must be specified. First, the minimum magnitude threshold above which the large earthquakes will be considered as characteristic, is adopted to be equal to 6.5 ($M_{thr\_I} \geq 6.5$), corresponding to a group of 670 ruptured cells. This threshold magnitude is selected to conform with the observed large events that occurred per segment (Fig. 4) and their magnitude uncertainties along with their fault dimensions (L, W). Since, is very likely that the resulting ruptures will be much larger than the sum of 670 cells, according to the geometrical properties of some segments (e.g. the fault dimensions of Ganos segment; Table 2) and the ability of the algorithm to allow fault interactions, an additional magnitude threshold equal to 7.0 ($M_{thr\_II} \geq 7.0$) corresponding to at least 2436 ruptured cells, is also considered. Then, the contribution of each segment to a single earthquake must be specified. Every earthquake that satisfies the first criterion is initially assigned to the segment where the nucleation starts. The same earthquake is also assigned to more segments, if the number of ruptured cells of another segment are at least the 75 per cent of the total number of its cells (in other words the rupture covers more than the 75 per cent of the segment's area) or if they exceed the minimum number of cells as previously defined, according to the magnitude threshold (670 and 2436 ruptured cells for the $M_{thr\_I} \geq 6.5$ and $M_{thr\_II} \geq 7.0$, respectively).

Considering the aforementioned criteria a detailed analysis of the ruptures of $M_{thr\_I} \geq 6.5$ and $M_{thr\_II} \geq 7.0$ earthquakes was carried out. Starting from the first magnitude threshold, 544 ruptures in total are produced in the simulated catalogue with occurrence rate equal to 0.054 earthquakes per year. Out of these, the 60 per cent of simulated earthquakes (322 earthquakes) are associated to single segment ruptures and the 40 per cent (213 earthquakes) with multisegmented ruptures. The latter number of ruptures can be separated into 69 pairs of simultaneously failed segments, 23 triple ruptures and a unique case where 4 out of 5 segments ruptured simultaneously. Counting each kind of ruptures per segment (Fig. 10a) some interesting features are observed. The Glafki bank segment is the only one that ruptured individually in the entire simulated catalogue, most probably due to its strike difference with the other four segments, and with $M_{max} = 6.7$ (Table 4). The other four segments (offshore Athos, Samothraki, Saros and Ganos) participate in both single and multiple ruptures with $M_{max} \geq 7.0$ (Table 4).

When the second magnitude threshold is considered, the total number of ruptures is significantly reduced, with only 192 ruptures associated with $M_{thr\_II} \geq 7.0$ earthquakes, during the 10 kyr of the simulation (0.019 earthquakes per year). The majority of these (63 per cent; 121 out of the 192 ruptures) are referred to multiple segmented ruptures (Fig. 10b). More specifically, the offshore Athos segment results in $M_w \geq 7.0$ earthquakes only in multiple ruptures, while Samothraki and Saros segments are ruptured individually only in one case. The Ganos segment is the only one where the $M_w \geq 7.0$ earthquakes are related to a large number of individual ruptures (37 single and 51 multiple ruptures, respectively; Table 4).

Focusing on the multiple ruptures per segment, it is found that offshore Athos participates in multiple ruptures 4 out of the total 34 times, resulting in $6.5 \leq M_w < 7.0$ earthquakes, whereas Samothraki has ruptured 41 times out of the total 81 times in the same magnitude range. On the other hand, the multiple ruptures of Saros and Ganos fault segments are mainly related to $M_w \geq 7.0$ earthquakes.

One more interesting observation in the simulated catalogue is the combination of the fault segments that participate in the multiple ruptures (an illustrated example of these combinations is shown in Fig. 11 for the first 2 kyr of the simulation). Table 5 shows all combinations that are found in the catalogue. The main pattern of these ruptures, even if they are 2- or 3-segment multiple ruptures, is that the neighbour fault segments are activated, as expected from the stress transfer triggering. Nevertheless, there are some extraordinary cases where the simultaneously failed segments are not adjacent. For example, the offshore Athos and Saros segments rupture together four times, without inclusion of the Samothraki

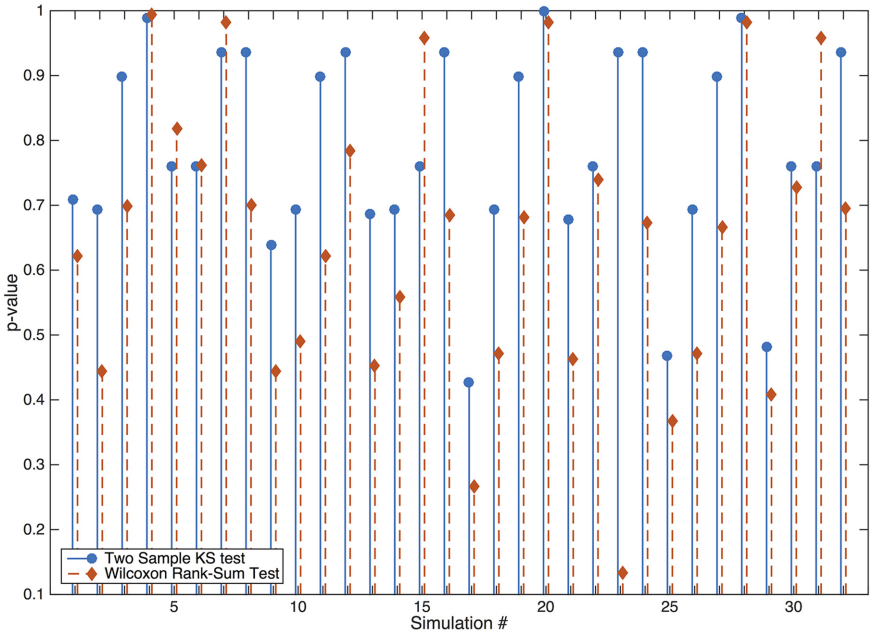

Figure 8. Calculated p-values of the two sample Kolmogorov–Smirnov (solid stems) and the Wilcoxon Rank–Sum (dashed stems) tests for the 32 simulated catalogues at 0.05 significance level ($\alpha = 0.05$).

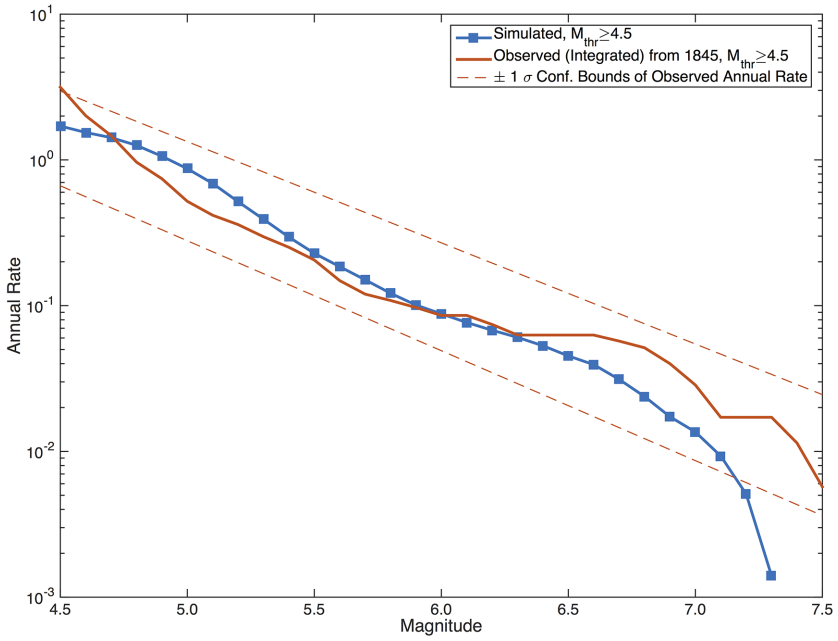

Figure 9. Annual occurrence rates of the observational integrated (since 1845) and the best performing simulated (Simulation 20; $\sigma = 0.06$ MPa, S–$R = 0.4$, A–$R = 7$; 10 kry) catalogues.

segment. In these cases, the fault segments not assigned in the multiple rupture are also participating in these ruptures, but with a smaller number of cells than the selected threshold number of cells for the characteristic earthquakes (e.g. with less than 670 cells for a $M = 6.5$ earthquake), playing a supportive role in the the rupture extent.

The earthquake recurrence times of each segment, participating in ruptures resulting either in $M_w \geq 6.5$ or in $M_w \geq 7.0$ simulated earthquakes, were studied by two different approaches. The goal of these approaches is to assess whether large earthquake occurrence in each segment is better described by a memoryless Poisson process or by a renewal process, which complies with the elastic rebound theory. The Poisson process can be expressed by the exponential distribution with probability density function (pdf) for interevent times data t as:

$$f\ (t T_r) = \frac{1}{T_r}\ \exp\left\{-\frac{t}{T_r}\right\}, \tag{3}$$

where T_r is the mean recurrence time in each data sample of large earthquakes above the magnitude threshold. The cumulative density

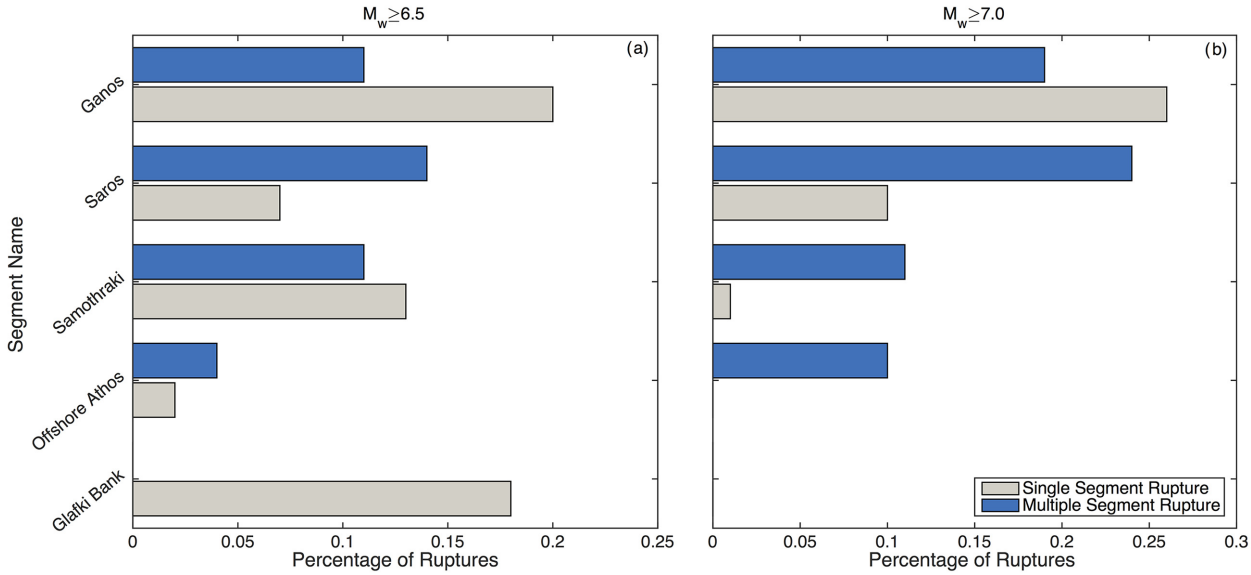

Figure 10. Percentage of both single and multiple ruptures of each segment of NATFZ obtained from the best performed simulated catalogue for both the $M_{\text{thr\_I}} \geq 6.5$ (a) and $M_{\text{thr\_II}} \geq 7.0$ (b) magnitude thresholds.

Table 4. Summary of the number of single and multiple ruptures for the magnitude thresholds $M_{\text{thr\_I}} \geq 6.5$ (544 ruptures in total) and $M_{\text{thr\_II}} \geq 7.0$ (192 ruprures in total) for each one of the five fault segments of NATFZ along with their maximum magnitude values obtained from the best performing 10 kyr simulated catalogue (simulation 20; $\sigma = 0.06$ MPa., S–$R = 0.4$, A–$R = 7$).

Fault Segment	$M_{\text{thr\_I}} \geq 6.5$		$M_{\text{thr\_II}} \geq 7.0$		$M_{\max}$
	Number of ruptures		Number of ruptures		
	Single	Multiple	Single	Multiple	
Glafki Bank	96	-	-	-	6.8
Offshore Athos	11	25	-	19	7.3
Samothraki	70	61	3	20	7.3
Saros	38	76	19	45	7.3
Ganos	110	57	49	37	7.3

function (cdf) of exponential distribution is then defined as:

$$F\ (t) = \ 1 - \exp\left\{-\frac{t}{T_r}\right\}. \tag{4}$$

For modelling large earthquake occurrence as a renewal process the BPT distribution (Matthews *et al.* 2002) is used. The pdf for interevent times t according to the BPT model is given by:

$$f\ (t\,T_r, \alpha) = \left(\frac{T_r}{2\pi\alpha^2 t^3}\right)^{1/2} \exp\left\{-\frac{(t-T_r)^2}{2T_r\alpha t}\right\}, \tag{5}$$

where T_r is the mean recurrence time and α the aperiodicity, which can be considered as the analog of the coefficient of variation of the normal distribution. It represents the level of variability expected around the long-term mean, T_r, in the model, taking values between 0 to 1 ($0 \leq \alpha \leq 1$) in order to address the physical meaning of the recurrence of large earthquakes. The cdf of BPT model is given by:

$$F\ (t) = \ \Phi\left[u_1\,(t)\right] + e^{2/a^2}\,\Phi\left[-u_2\,(t)\right], \tag{6}$$

where $\Phi(\cdot)$ is the cdf of the normal distribution, and u_1 and u_2 are defined as follows:

$$u_1 = a^{-1}\ \left[t^{1/2}{T_r}^{-1/2} - t^{-1/2}{T_r}^{1/2}\right] \tag{7}$$

$$u_2 = a^{-1}\ \left[t^{1/2}{T_r}^{-1/2} + t^{-1/2}{T_r}^{1/2}\right]. \tag{8}$$

The comparison of the models is made in terms of the Akaike (Akaike 1974) Information Criterion (AIC; Appendix A2) values after calculating the corresponding log-likelihood values. The log–likelihood function of the Poisson process is defined by:

$$ln\ L_P = (N-1)\ \ln\left(\frac{1}{T_r}\right) - \frac{t_N}{T_r}, \tag{9}$$

where N is the number of observations and t_N is the occurrence time of the last event in the data sample, and the log-likelihood function of the BPT (or any other renewal model) is given by:

$$ln\ L_{BPT} = \sum_{j=1}^{N-1} \ln\left\{\frac{f\,(\Delta t\,(j))}{1 - F\,(t \leq \Delta t\,(j))}\right\} - \frac{t_N}{T_r}, \tag{10}$$

where $\Delta t(j)$ is the interevent time between the jth and the jth+1 events and $f(\Delta t)$ and $F(t \leq \Delta t)$ are the pdf and cdf of the BPT distribution, respectively (eqs 5 and 6, respectively). The non parametric Anderson–Darling goodness of fit test (AD test; Appendix 2) is further applied, aiming to measure the differences among the empirical cumulative density function (ecdf) as obtained from each data set and the cdfs of the BPT and Poisson model (eqs 4 and 6).

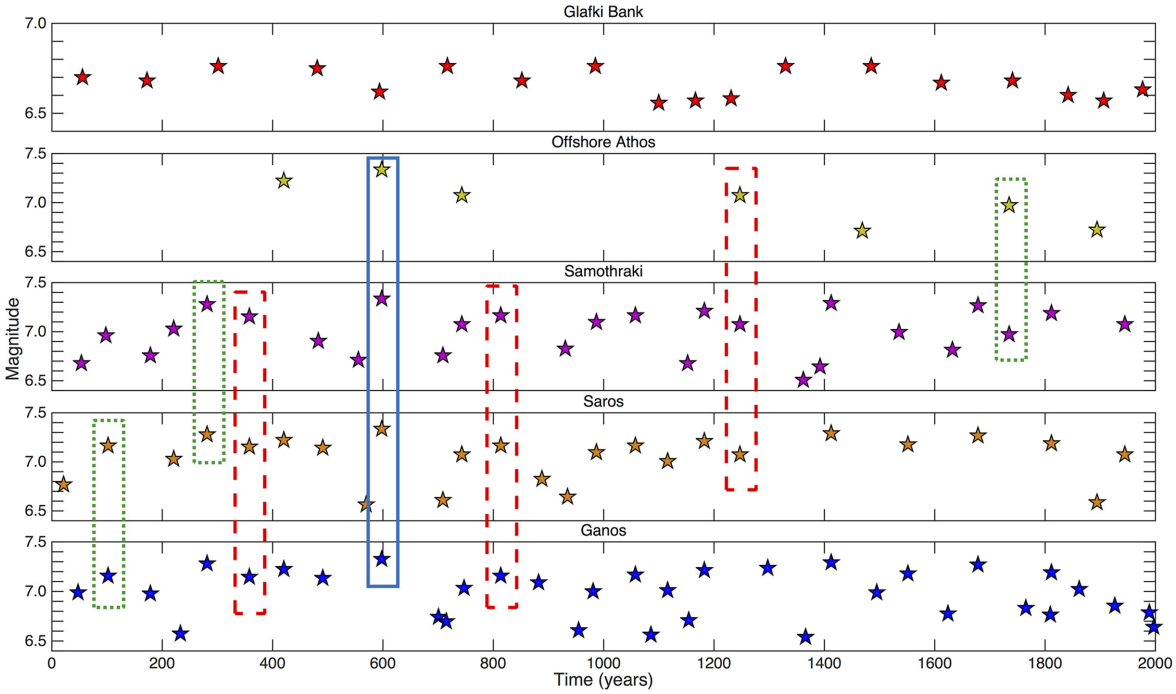

Figure 11. Snapshot of the first 2 kyr temporal distribution of the $M_w \geq 6.5$ earthquakes of the best performed simulated catalogue. Dotted and dashed boxes indicate some of the combinations of the 2 and 3 fault segment ruptures, respectively, while the solid one indicates the unique case of the four segment rupture.

Table 5. Number of 2, 3 and 4 segments multiple ruptures for all the combinations of the participating fault segments of NATFZ.

2-Segments ruptures		3-Segments ruptures		4-Segments ruptures	
Fault segments	Number of ruptures	Fault segments	Number of ruptures	Fault segments	Number of ruptures
Offshore Athos - Samothraki	18	Offshore Athos - Samothraki - Saros	3	Offshore Athos - Samothraki - Saros - Ganos	1
Offshore Athos - Saros	2	Offshore Athos - Saros - Ganos	1		
Samothraki - Saros	15	Samothraki - Saros - Ganos	22		
Samothraki - Ganos	2	Offshore Athos – Samothraki - Ganos	1		
Saros - Ganos	30				

Table 6. Statistical parameters (mean recurrence time; *Tr*, standard deviation; σ and coefficient of variation; C_v) of the five segments of NATFZ as obtained from the best performing simulated catalogue (simulation 20 in Table 3; $\sigma = 0.06$ MPa, S–$R = 0.4$, A–$R = 7$) for both the magnitude thresholds adopted for the recurrence modelling, along with the number of observations (N_{obs}) of interevent times used in the calculations.

Fault segment	$M_{thr\_I} \geq 6.5$				$M_{thr\_II} \geq 7.0$			
	Nobs	*Tr* (yr)	σ (yr)	C_v	Obs.	*Tr* (yr)	σ (yr)	C_v
Glafki Bank	95	104.64	35.04	0.33	-	-	-	-
Offshore Athos	35	272.34	144.35	0.53	18	520.94	349.39	0.67
Samothraki	130	76.15	29.82	0.39	22	375.54	272.36	0.72
Saros	113	87.88	30.56	0.34	63	154.27	95.86	0.62
Ganos	166	59.60	38.93	0.48	85	116.40	39.31	0.34

As a first step before the application of statistical models, the mean recurrence time, T_r, of each fault segment along with its standard deviation (σ) and the corresponding coefficient of variation (C_v) are calculated, for both magnitude thresholds wherever it is possible (Table 6). The mean T_r obtained for the $M_{thr\_I} \geq 6.5$ simulated earthquakes varies from almost 60 to 272 yr, depending on the long–term slip rate values of the segments. The Glafki bank and offshore Athos segments exhibit the larger values of T_r equal to 104.76 and 272.34 yr, respectively, since their slip rates are the lowest along NATFZ. The other three segments (Samothraki, Saros and Ganos), with higher slip rates, are more frequently failed in earthquakes above the M_{thr_I}. In all these cases, either for larger or intermediate

Table 7. MLE parameters estimates of the BPT (T_r and α) and exponential (T_r) models, along with their respective 95 per cent confidence intervals for the five fault segments of NATFZ for both magnitude thresholds adopted for the recurrence modelling.

Fault segment	$M_{\text{thr\_I}} \geq 6.5$		$M_{\text{thr\_II}} \geq 7.0$	
	Exponential model	BPT model	Exponential model	BPT model
Glafki Bank	T_r= 104.64 (86.42,129.34)	T_r= 104.74 (97.56,111.72)α = 0.34(0.28,0.38)	-	-
Offshore Athos	T_r= 272.34 (200.62,390.99)	T_r= 272.05 (226.11,318.56)α = 0.51 (0.38,0.64)	T_r= 520.94 (344.50,878.98)	T_r= 520.57 (356.98,684.89)α = 0.68(0.43,0.93)
Samothraki	T_r= 76.15 (64.59,91.15)	T_r= 76.21(70.42,81.89)α = 0.44 (0.39,0.49)	T_r= 375.55(257.38,599.25)	T_r= 376.41 (255.31,495.77)α = 0.77(0.51,1.00)
Saros	T_r= 87.88 (73.69,106.64)	T_r= 87.91 (80.12,95.66)α = 0.48 (0.41,0.54)	T_r= 154.27 (122.28,200.76)	T_r= 154.35 (134.12,174.42)α = 0.53(0.43,0.63)
Ganos	T_r= 59.60 (51.48,69.82)	T_{r} = 59.59 (52.35,66.86)α = 0.80 (0.70,0.89)	T_r= 116.40 (95.14,145.73)	T_r= 126.27 (108.14,124.66)α = 0.33(0.28,0.38)

mean T_r, the values of C_v, which range between 0.33 and 0.53 (Table 6), evidence a quasi-periodic recurrence behaviour. The earthquakes with $M_{\text{thr\_II}} \geq 7.0$ appear considerably less frequent. The T_r for the four such cases range from slightly above a century (Ganos segment; T_r= 116.40 yr) to the extreme value of about four and five centuries in Samothraki (T_r = 375.54 yr) and offshore Athos (T_r = 520.94 yr) segments, respectively. Their corresponding C_v values also suggest quasi periodic behaviour for the Ganos segment (0.34) and a more aperiodic (larger level of variability of T_r) for the offshore Athos (C_v= 0.67), Samothraki (C_v= 0.72) and Saros (C_v= 0.62) segments.

In the next step, the Poisson and the BPT models (eqs 3 and 5, respectively) are applied in each data sample of interevent times (ΔT). The parameters of both models are estimated via the MLE method according to their respective formulations (eqs 9 and 10). The 95 per cent confidence intervals of the parameters in each case are estimated as well. Results of the MLE implementation are given in Table 7. The maximum likelihood estimates of the mean recurrence time, T_r, for the Exponential model are equal to each data samples mean values for both magnitude thresholds, as expected.

The optimal set of the BPT parameters (T_r, α) that maximize the likelihood function (Figs 12 and 13) exhibiting slight or more significant differences in respect to the sample statistics in most of the cases. The only case in which the optimal set of the estimated parameters are almost equal to the sample statistics is the one of Glafki bank fault segment's data set of $M_{\text{thr\_I}} \geq 6.5$ earthquakes. Specifically, the MLE estimates are found to be equal to T_r= 104.74 yr and α = 0.34, instead of sample values equals to 104.64 yr and 0.33, for the mean recurrence time and the coefficient of variation, respectively.

In contrary, the MLE results for the other cases and for both magnitude thresholds ($M_{\text{thr\_I}} \geq 6.5$ and $\text{M}_{\text{thr\_II}} \geq 7.0$) differ from the sample statistics. For example, the Saros fault segment's data of $M_{\text{w}} \geq 7.0$ results in optimal values equal to T_r = 154.35 yr and α = 0.53, instead of the samples mean and C_v, equal to 154.27 yr and 0.62, respectively. The most significant discrepancy is observed in the case of the Ganos fault segment for the interevent times of $M_{\text{thr\_I}} \geq 6.5$ earthquakes. Specifically, the MLE estimate of aperiodicity for this case is found equal to 0.80 with its 95 per cent confidence interval ranging from 0.70 to 0.89, whereas the sample's $C_v$equals to 0.48. This significant difference among the values results in a high variable recurrence model according to the MLE estimation, instead of a quasi-periodic one in accordance to the sample statistics. The optimal estimated models for the data samples of $M_{\text{thr\_I}} \geq 6.5$ and $M_{\text{thr\_II}} \geq 7.0$ earthquakes are shown in Figs 14 and 15, respectively.

The performance of each model is then quantitatively measured by the calculation of their AIC (Appendix A2) values (Table 8). Additionally, results of the Anderson–Darling test are shown in Table 9. The results of AIC calculations reveal that the BPT model performs better than the Poisson model in all data sets and for both magnitude thresholds. In more detail, the BPT model performs significantly better than the Poisson model in many cases such as the Glafki bank segment for $M_{\text{thr\_I}} \geq 6.5$ earthquakes, in which the values of AIC are equal to 1075.60 and 934.72, respectively. On the contrary, there are cases where the differences among the AIC of the two models are not significant. These cases are related with Ganos segment for earthquakes with $M_{\text{thr\_I}} \geq 6.5$, which is clearly not near the characteristic magnitude threshold in accordance with its dimensions, and Samothraki segment for the $M_{\text{thr\_II}} \geq 7.0$ earthquakes.

The results of the AD test further support the conclusions because its statistics show significantly better performance of the BPT model against the Poisson model for the $M_{\text{thr\_I}} \geq 6.5$ earthquakes (in four out of the five cases the BPT statistic is below the critical value, in contrast to the Poisson model that is significantly larger). The case of Ganos fault segment data for $M_{\text{thr\_I}} \geq 6.5$ threshold is the only one in which the test rejects both the Exponential and BPT models (Table 9). This happens because the optimal BPT model exhibits high aperiodic behaviour (α = 0.80), quite similar to the Exponential model.

However, when the $M_{\text{thr\_II}} \geq 7.0$ is considered, the comparison exhibits significantly better performance of the renewal model against the Poisson one for all the cases and for both tests. These conclusions could be easily interpreted from the visual comparisons among the cumulative density functions of Figs 16 and 17. The summary of the results of the statistical analysis shows that a renewal model, the BPT in this study, performs better than the Poisson in the modelling of the recurrence time of large earthquakes in all segments of NATFZ, suggesting that an elastic rebound motivated behaviour is more likely than the memoryless one. The rejection of both models for the case of $M_{\text{thr\_I}} \geq 6.5$ earthquakes interevent data indicates that the consideration of only the $M_{\text{thr\_I}} \geq 7.0$ threshold for the sample of Ganos fault segment under the characteristic earthquake hypothesis could be possibly more proper, due to its significantly larger length than the other segments ones.

6 DISCUSSION AND CONCLUSIONS

The application of the physics-based simulator algorithm in the five fault segments of NATFZ has allowed the compilation of a simulated seismic catalogue lasting 10 kyr and containing 17 069 events

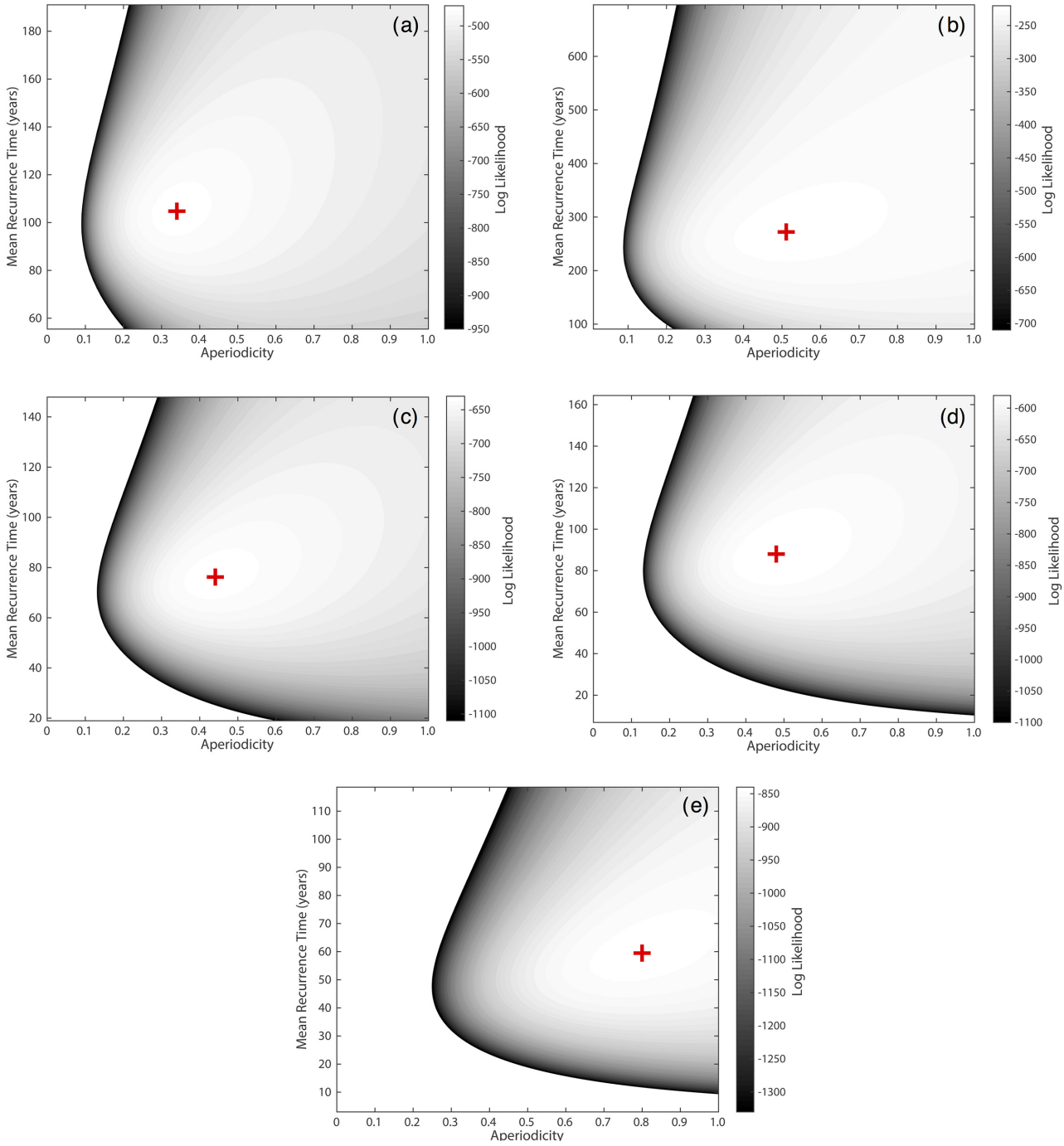

Figure 12. BPT model's likelihood plots of the interevent times data of large simulated earthquakes with $M_{\text{thr\_I}} \geq 6.5$ for the Glafki bank (a), offshore Athos (b), Samothraki (c), Saros (d) and Ganos (e) fault segments. Likelihood values are shown in accordance to the respective colour bar. Crosses are indicating the optimal set of parameters T_r and α.

with $M_w \geq 4.5$. Particularly, the number of earthquakes with $M_w \geq 6.5$ is equal to 544, providing the ability for a thorough study of their recurrence properties. This provides adequate catalogue duration for achieving a sufficient number of large events per certain fault segment, because this number is very limited in the observational historical catalogues (Table 1). For example, only one earthquake with $M_w \geq 6.5$ has occurred since 1845 in both Glafki Bank and Ganos segments, in the westernmost and easternmost parts of NATFZ, respectively.

The simulated catalogue manages to replicate the observed seismicity successfully, as the *b*-value and the annual earthquake occurrence rates estimates are very similar in comparison with the observational ones. The good agreement of the simulated and observed annual rates further support the consideration that the seismic contribution accounts for almost 60 per cent of the geodetically measured rate. Some mismatches are observed in the rates of the $M_w \geq 6.5$ earthquakes and in the values of maximum magnitude per segment. These differences may be ascribed to the fact that most

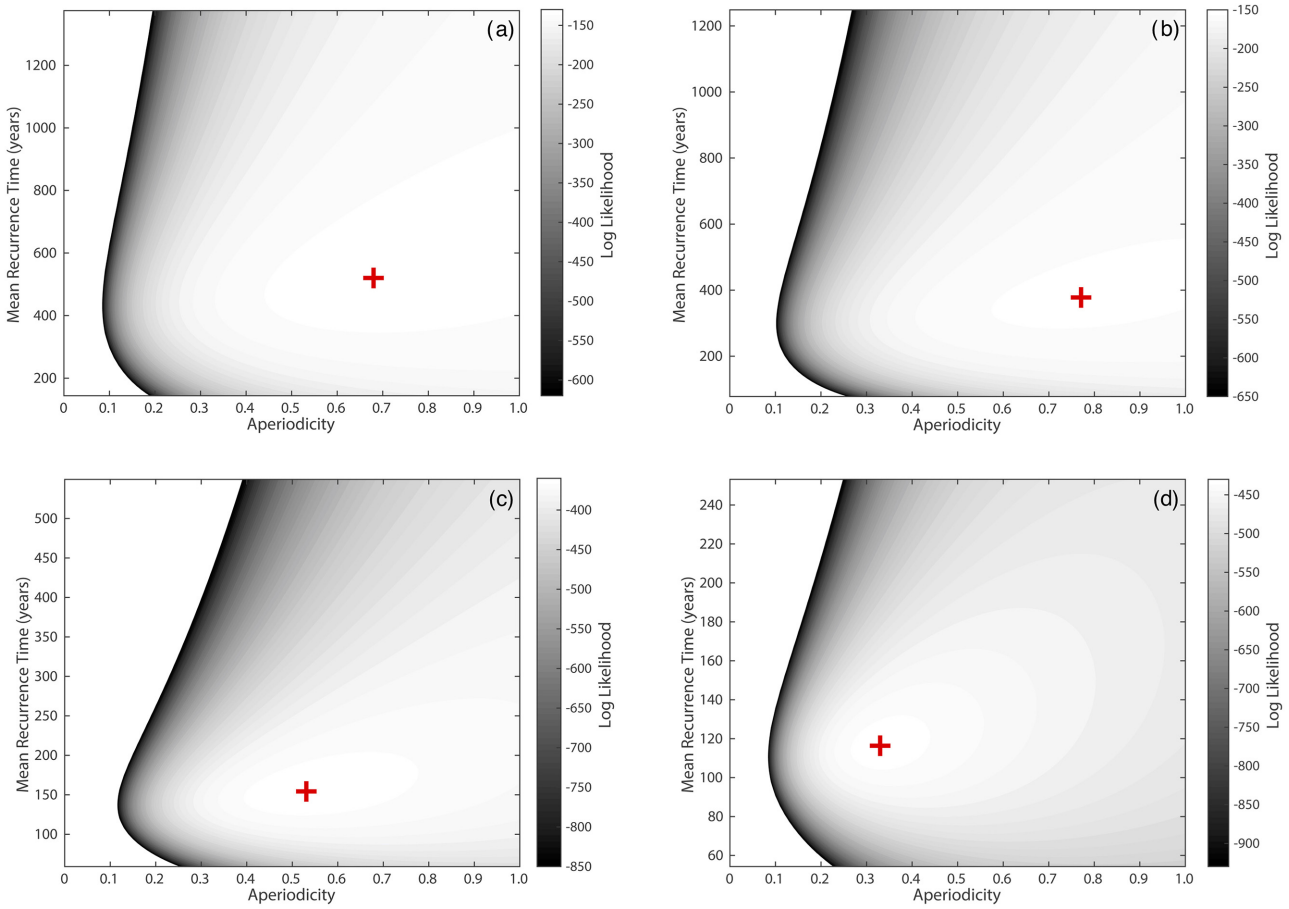

Figure 13. BPT model's likelihood plots of the interevent times data of large simulated earthquakes with $M_{\text{thr\_II}} \geq 7.0$ for the offshore Athos (a), Samothraki (b), Saros (c) and Ganoss fault segments. Likelihood values are shown in accordance to the respective colour bar. Crosses are indicating the optimal set of parameters T_r and α.

of the large earthquakes of the observational catalogue belong to the historical or the early instrumental period, with their magnitudes being possibly overestimated. An example is the magnitude of the 1905 $M_w = 7.5$ earthquake that occurred on the offshore Athos fault segment. Looking at the ISC–GEM (ISC 2019) instrumental earthquake catalogue, its estimated magnitude is given to $M_w = 7.24$, in very good agreement with the largest magnitude that is reported in the simulated catalogue for this segment. This supports the assumption of magnitude overestimation in the historical catalogue. Nevertheless, in this study all magnitudes are taken from the catalogue of Papazachos & Papazachou (2000) for the sake of homogeneity of the integrated observational catalogue, in which the magnitude of large earthquakes even if they are historical or early instrumental were converted with the same method according to the relevant relations of Papazachos *et al.* (1997a) as mentioned in Section 2. The main trend of the large magnitude earthquakes of the simulated catalogue is to coincide with the lower confidence bound (the -1σ of reported magnitude) of the observational one.

Emphasizing the large earthquakes occurrence, both single and multiple segmented ruptures are reported in the simulated catalogue. A remarkable point arising from the results of the multiple ruptures is that the segments with larger and similar slip rates (13, 13 and 13.5 mm yr^{-1} for the Samothraki, Saros and Ganos segments, respectively) participate more frequently in simultaneous ruptures than the offshore Athos segment, whose slip rate is lower (7.5 mm yr^{-1}). This agrees with Scholz (2010) who suggests that fault synchronization and rupture jumping phenomena are more likely in segments with equal or similar slip rate values.

The mean recurrence time, T_r, for both magnitude thresholds, $M_{\text{thr\_I}} \geq 6.5$ and $M_{\text{thr\_II}} \geq 7.0$, exhibit large fluctuations from the one fault segment to the other. This fact could be an index about their possible characteristic magnitudes. More specifically, the short values of sample mean $T_r$in Samothraki, Saros and Ganos segments (76.15, 87.88 and 59.60 yr, respectively) for $M_{\text{thr\_I}} \geq 6.5$ earthquakes indicate that their characteristic magnitude is more likely to be larger. This assumption is confirmed when the higher magnitude threshold, $M_{\text{thr\_I}} \geq 7.0$, is considered. The resulting T_r in this case are equal to 375.54 yr for Samothraki, 154.27 yr for Saros and 116.40 yr for Ganos segment, which are reliable values and in accordance with the time needed for stress accumulation and release for such large earthquakes. The MLE parameter estimation for both models is implemented for further statistical analysis of the interevent times of large earthquakes for both magnitude thresholds, $M_{\text{thr\_I}} \geq 6.5$ and $M_{\text{thr\_II}} \geq 7.0$. Some discrepancies are observed among the MLE estimates of the BPT parameters and the corresponding sample statistics. These discrepancies are mainly observed among the aperiodicity, α, of the BPT model and the arithmetic C_v values. In this respect, the optimal BPT models exhibit larger variability around T_r.

The applied tests (AIC and AD) reveal a considerably better performance of the renewal BPT model than the memoryless Poisson

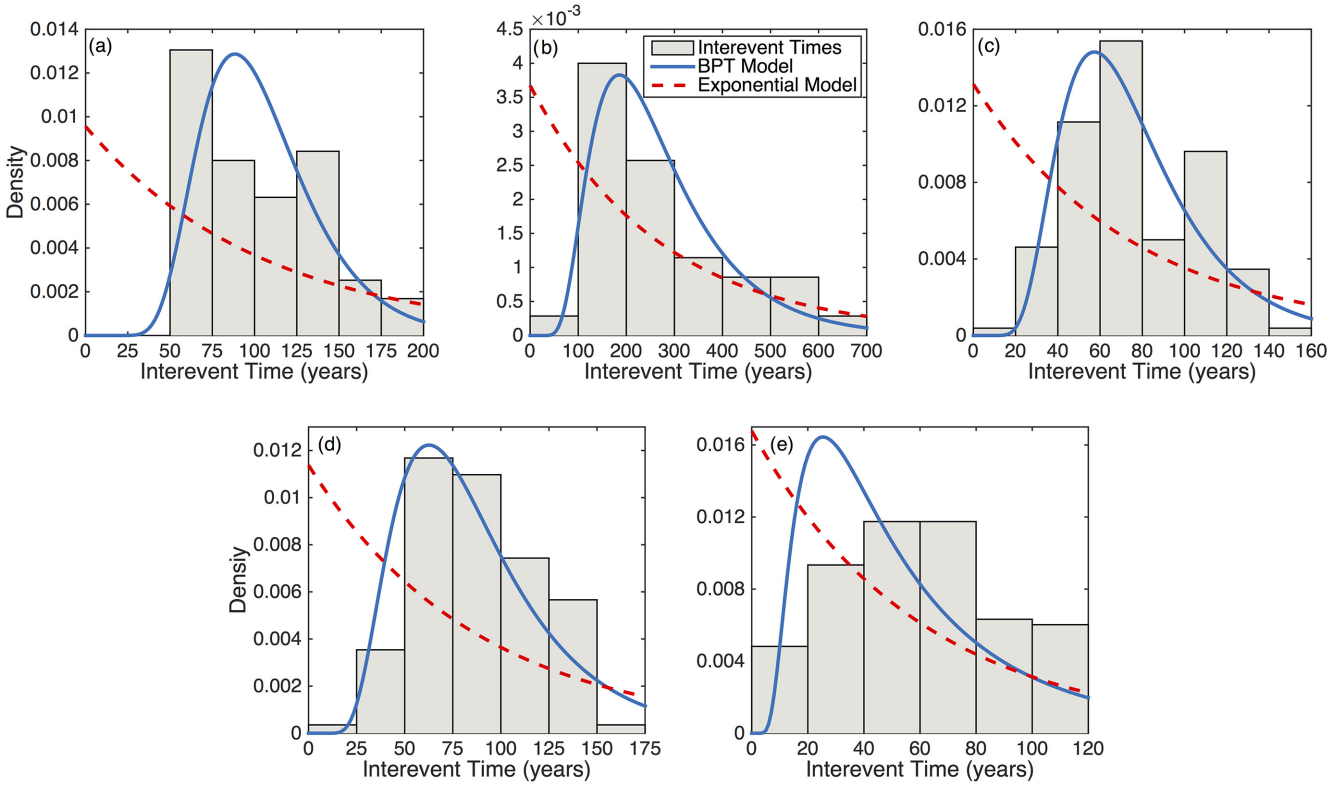

Figure 14. Probability density functions of Exponential (dashed line) and BPT (solid line) models for the interevent times of large earthquakes with $M_{\text{thr\_I}} \geq 6.5$ for the Glafki bank (a), offshore Athos (b), Samotrhaki (c), Saros (d) and Ganos (e) fault segments.

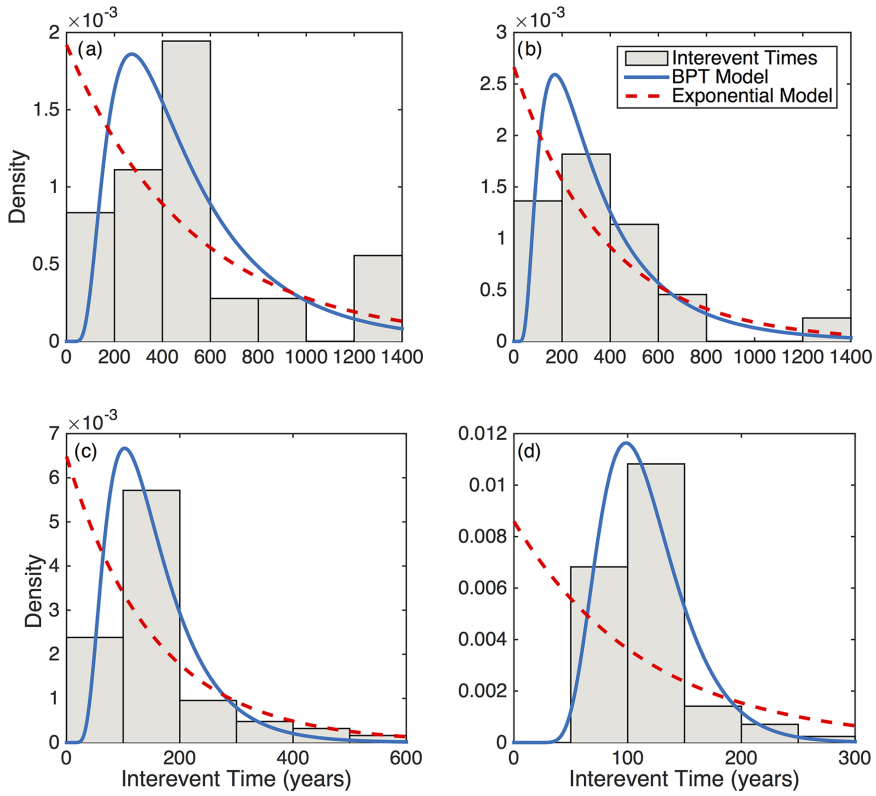

Figure 15. Probability density functions of exponential (dashed line) and BPT (solid line) models for the interevent times of large earthquakes with $M_{\text{thr\_II}} \geq 7.0$ for the offshore Athos (a), Samotrhaki (b), Saros (c) and Ganos (d) fault segments.

Table 8. Log-likelihood and AIC calculated values of the Poisson ($\ln L_P$ and AIC_P, respectively) and the Renewal ($\ln L_R$ and AIC_R, respectively) models for the five segments of NATFZ for both magnitude thresholds adopted for the recurrence modelling.

Fault segment	$M_{thr\_I} \geq 6.5$				$M_{thr\_II} \geq 7.0$			
	$\ln L_P$	$\ln L_R$	AIC_P	AIC_R	$\ln L_P$	$\ln L_R$	AIC_P	AIC_R
Glafki Bank	–536.80	–465.36	1075.60	934.72	-	-	-	-
Offshore Athos	–231.25	–216.08	464.50	436.16	–130.60	–126.00	263.20	256.00
Samothraki	–693.26	–624.38	1388.52	1252.76	–152.42	–148.17	306.84	300.34
Saros	–618.79	–570.52	1239.58	1145.04	–380.44	–353.85	762.80	711.70
Ganos	–844.56	–834.63	1691.12	1673.26	–489.35	–424.94	980.70	853.88

Table 9. Anderson–Darling test statistics of the Poisson and the Renewal models for the five fault segments of NAT for both magnitude thresholds adopted for the recurrence modelling at 5 per cent level of significance.

Fault segment	$M_{thr\_I} \geq 6.5$			$M_{thr\_II} \geq 7.0$		
	AD statistic BPT model	AD statistic exponential model	Critical value	AD statistic BPT model	AD statistic exponential model	Critical value
Glafki Bank	1.866	19.787	2.494	-	-	-
Offshore Athos	0.505	4.231	2.497	0.352	1.521	2.503
Samothraki	1.061	21.118	2.493	0.334	1.126	2.501
Saros	2.439	20.993	2.493	1.293	8.402	2.495
Ganos	9.154	16.838	2.493	0.523	18.384	2.494

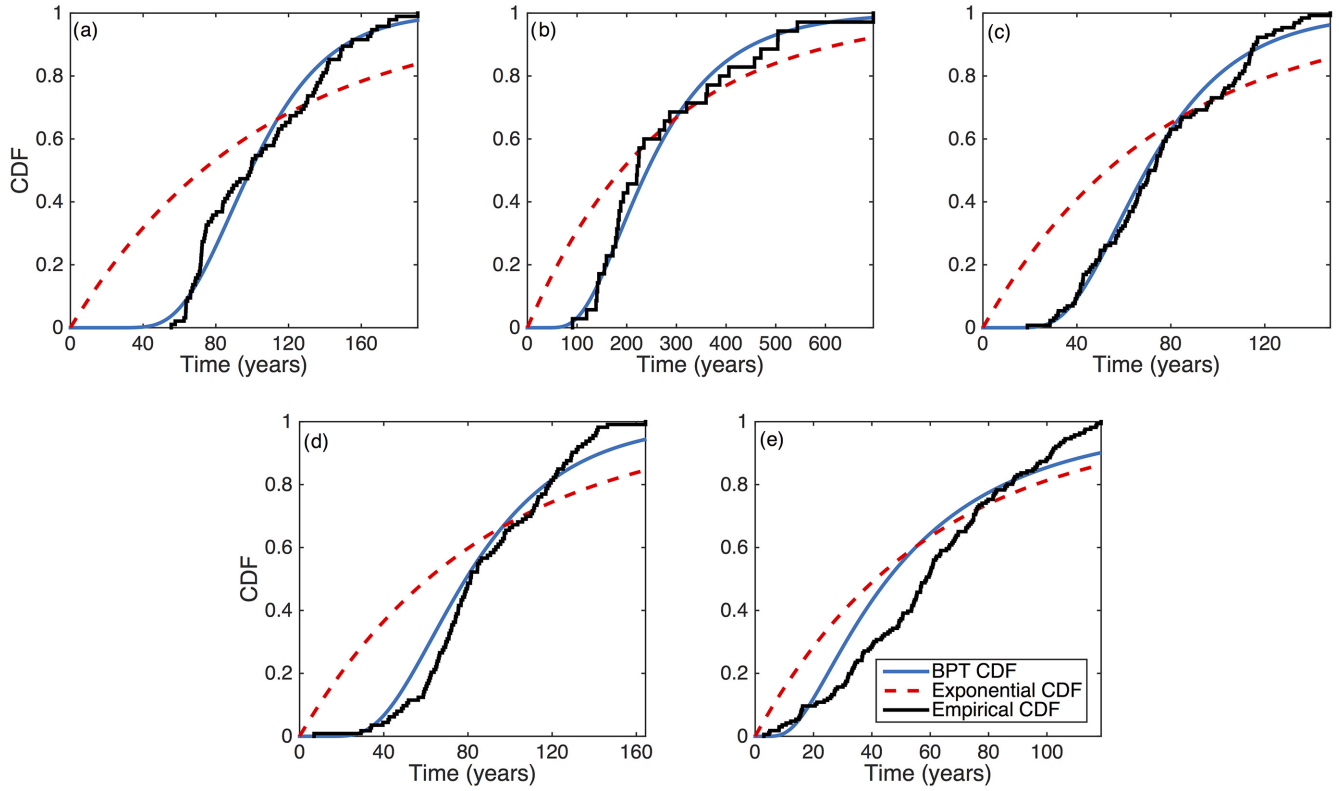

Figure 16. Comparison of empirical cdf (solid black lines) and the cdfs of the BPT (solid bright lines) and exponential model (dashed lines) for the Glafki bank (a), offshore Athos (b), Samothraki (c), Saros (d) and Ganos (e) fault segments considering the interevent times of the $M_{thr\_I} \geq 6.5$ earthquakes.

model in all NATFZ segments, except the one of the Ganos segment for $M_{thr\_I} \geq 6.5$, agreeing with elastic rebound theory for the occurrence of large earthquake and quasi-periodic recurrence behaviour. The poor fit of both models, as obtained by the MLE implementation, for the $M_{thr\_I} \geq 6.5$ earthquakes in Ganos fault segment indicate that the $6.5 \leq M_w < 7.0$ simulated earthquakes could not be possibly considered as near characteristic ones but ruptured smaller patches of the fault segment.

These results provide information about the occurrence of large earthquakes in NATFZ and could have many potential uses in combination with additional seismic data as an input parameter in modern time-independent and time-dependent seismic hazard assessment investigations, such as the development of ERF over a specific time span based on single and multiple rupture scenarios. Specifically, for joint rupture scenarios (simultaneous ruptures of multiple segments) the current result could provide information on

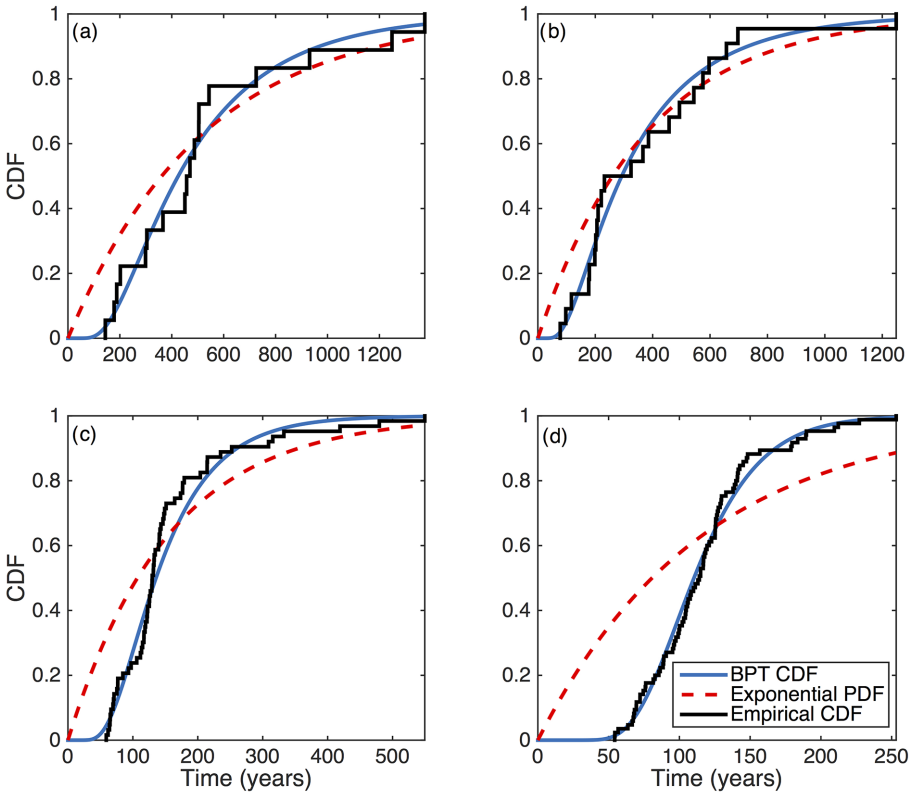

Figure 17. Comparison of empirical cdf (solid black lines) and the cdfs of the BPT (solid bright lines) and Exponential model (dashed lines) for the offshore Athos (a), Samothaki (b), Saros (c) and Ganos (d) fault segments considering the interevent times of the $M_{\text{thr\_II}} \geq 7.0$ earthquakes.

quantifying the weights of the possible rupture scenarios. A simple strategy concerning the weighting of rupture scenarios along NATFZ could be derived by dividing the number of times that a certain joint rupture is reported in the simulated catalogue with the total number of the same kind of joint ruptures (Table 4) for a specific magnitude threshold (e.g. $M_{\text{w}} \geq 6.5$). For example, in the case of 2 segment ruptures for the $M_{\text{w}} \geq 6.5$ earthquakes the total number of ruptures are equal to 67, whereas the scenario of offshore Athos and Samothraki segments rupturing together is reported 18 times. In contrast, the Samothaki and Ganos scenario is reported only two times. From these numbers one can obtain the relative ratios, that are equal to 0.26 and 0.03 for offshore Athos and Samothraki and Samothaki and Ganos rupture scenarios, respectively, that could latter on be used as weights. Alternatively, an equal weighting approach could also be used for the possible rupture scenarios.

ACKNOWLEDGEMENTS

The constructive and detailed comments of Prof R. Zuniga, Dr D. Fitzenz and Dr D.P. Schwartz are greatly appreciated and contributed to the significant improvement of the manuscript. Gratitude is also extended to Dr M. Segou for her editorial assistance and constructive suggestions. CK, EP and VK would like to acknowledge the financial support of the project 'HELPOS – Hellenic System for Lithosphere Monitoring' (MIS 5002697) which is implemented under the Action 'Reinforcement of the Research and Innovation Infrastructure', funded by the Operational Programme 'Competitiveness, Entrepreneurship and Innovation' (NSRF 2014–2020) and co-financed by Greece and the European Union (European Regional Development Fund). The historical and instrumental earthquake catalogues of Geophysics Department of the Aristotle University of Thessaloniki (http:/geophysics.geo.auth.gr/ss) and the instrumental ISC-GEM catalogue provided by the International Seismic Centre (http://www.isc.ac.uk/iscgem/index) are used in this study. The maps and graphs are generated using the GMT software (Wessel *et al.* 2013) and MATLAB software (http://www.mathworks.com/products/matlab). Fault plane solutions data used in this paper came from https://www.globalcmt.org/ and other resources listed in the References Section. Geophysics Department Contribution 941.

REFERENCES

Akaike, H., 1974. A new look at the statistical model identification, *IEEE Trans. Autom. Control,* **AC-19,** 716–723.

Aki, K., 1965. Maximum likelihood estimation of b in the formula log n = a – bm and its confidence limits, *Bull. Earthq. Res. Inst. Tokyo Univ.,* **43,** 237–239.

Aksoy, M.E., Meghraoui, M., Vallee, M. & Ziyadin, C., 2010. Rupture characteristics of the A.D. 1912 Murefte (Ganos) earthquake, segment of the North Anatolian fault (western Turkey), *Geology,* **38**(11), 991–994.

Ambraseys, N., 2002. The seismic activity of the Marmara Sea Region over the last 2000 years, *Bull. seism. Soc. Am.,* **92**(1), 1–18.

Ambraseys, N., 2009. *Earthquakes in the Eastern Mediterranean and the Middle East: A Multidisciplinary Study of 2000 Years of Seismicity,* Cambridge Univ. Press, 947pp.

Ambraseys, N. & Jackson, J.A., 2000. Seismicity of the Sea of Marmara (Turkey) since 1500, *Geophys. J. Int.,* **141,** F1–F6.

Aristotle University of Thessaloniki, 1981. *Aristotle University of Thessaloniki Seismological Network.* International Federation of Digital Seismograph Networks, doi:10.7914/SN/HT.

Armijo, R., Meyer, B., Hubert, A. & Barka, A., 1999. Westward propagation of the North Anatolian fault into the northern Aegean: timing and kinematics, *Geology,* **27**(3), 267–270.

Armijo, R., Meyer, B., Navarro, S., King, G. & Barka, A., 2002. Asymmetric slip partitioning in the Sea of Marmara pull-apart: a clue to propagation processes of the North Anatolian Fault?, *Terra Nova,* **14,** 80–86.

Berryman, K., *et al.*, 2012. Late Holocene rupture history of the Alpine Faults in South Westland, New Zealand , *Bull. Seism. Soc. Am.,* **102**(2), 620–638.

Biasi, G. P., Weldon, R. J., II., Fumal, T. E. & Seitz, G. G., 2002. Paleoseismic event dating and the conditional probability of large earthquakes on the Southern San Andreas Fault, California, *Bull. seism. Soc. Am.,* **92,** 2761–2781.

Biasi, G.P., Langridge, R. M., Berryman, K. R., Clark, K. J. & Cochran, U. A., 2015. Maximum-likelihood recurrence parameters and conditional probability of a ground-rupturing earthquake on the southern Alpine fault, South Island, New Zealand, *Bull. seism. Soc. Am.,* **105,** 96–106.

Bulut, F., Ozener, H., Dogru, A., Aktug, B. & Yaltirak, C., 2008. Structural setting along the Western North Anatolian Fault and its influence on the 2014 North Aegean Earthquake (M_w 6.9), *Tectonophysics,* **745,** 382–394.

Christophersen, A., Rhoades, D.A. & Colella, H.V., 2017. Precursory seismicity in regions of low strain rate: insights from a physical-based earthquake simulator, *Geophys. J. Int.,* **209,** 1513–1525.

Console, R., Carluccio, R., Papadimitriou, E. & Karakostas, V., 2015. Synthetic earthquake catalogs simulating seismic activity in the Corinth Gulf, Greece, fault system, *J. geophys. Res.,* **120,** 326–343.

Console, R., Nardi, A., Carluccio, R., Murru, M, Falcone, G. & Parsons, T., 2017. A physics-based earthquake simulator and its application to seismic hazard assessment in Calabria (Southern Italy) region, *Acta Geophys*., **65,** 243–257.

Console, R., Vannoli, P. & Carluccio, R., 2018a. The seismicity of Central Apennines (Italy) studied by means of a physics-based earthquake simulator, *Geophys. J. Int.,* **212,** 916–929.

Console, R., Chiappini, M., Minelli, L., Speranza, F., Carluccio, R. & Greco, M., 2018b, Seismic hazard in southern Calabria (Italy) based on the analysis of a synthetic earthquake catalog, *Acta Geophys*., **66,** 931–943.

Console, R., Murru, M., Vannoli, P., Carluccio, R., Taroni, M. & Falcone, G., 2020, Physics-based simulation of sequences with multiple mainshocks in Central Italy, *Geophys. J. Int.,* **223,** 526–542.

Davis, R., England, P. & Parsons, B., 1997. Geodetic strain of Greece in the interval 1892–1992, *J. geophys. Res.,* **102**(24), 571–24, 588.

Dieterich, J.H., 1994. A constitutive law for rate of earthquake production and its application to earthquake clustering, *J. geophys. Res.,* **99,** 2601–2618.

Ellsworth, W. L., Matthews, M. V., Nadeau, R. M., Nishenko, S. P., Reasenberg, P. A. & Simpson, R. W., 1999. A physically based earthquake recurrence model for estimation of long-term earthquake probabilities, *U.S. Geol. Surv. Open-File Rept.,* 99–522.

Field, E.H. *et al.* 2014. Uniform California Earthquake Rupture Forecast, Version 3 (UCERF3)–The Time-Independent Model, *Bull. seism. Soc. Am.,* **104,** 1122–1180. doi:10.1785/0120130164.

Field, E.H. *et al.* 2015. Long-term time-dependent probabilities for the third uniform California earthquake rupture forecast (UCERF3), *Bull. seism. Soc. Am.,* **105,** 511–543. doi:10.1785/0120140093.

Field, E.H., 2015. Computing elastic-rebound-motivated earthquake probabilities in unsegments fault models: a new methodology supported by physics-based simulators, *Bull. seism. Soc. Am.,* **105,** 544–559. doi:10.1785/01201140094.

Field, E.H., 2019. How physics-based earthquake simulators might help improve earthquake forecasts, *Seismol. Res. Lett.,***90**(2A), 467–472.

Fitzend, D.D. & Nyst, M., 2015. Building time-dependent earthquake recurrence models for probabilistic risk computations, *Bull. seism. Soc. Am.,* **105,** 120–133.

Fitzenz, D.D., 2018. Conditional probability of what? Example of Nankai Interface in Japan, *Bull. seism. Soc. Am.,* **108**(6), 3169–3179.

Floyd, M.A. *et al.* 2010. A new velocity field for Greece: implications for the kinematics and dynamics in Aegean, *J. geophys. Res.,* **115,** B10403. doi: 10.1029 /2009JB007040.

Hardebeck, J.L., 2004. Stress triggering and earthquake probability estimates, *J. geophys. Res.,* **109,** B04310. doi:10.1029/2003JB002437.

Harris, R.A., 1998. Introduction to special section: stress triggers, stress shadows, and implications for seismic hazard, *J. geophys. Res.,* **103**(24), 346–24, 358.

Harris, R.A. & Simpson, R.W., 1998. Suppression of large earthquakes by stress shadows: a comparison of Coulomb and rate-and-state failure, *J. geophys. Res.,* **103**(24), 439–24, 451. doi:10.1029/98JB00793.

Hatzfeld, D., Ziazia, M., Kementzetzidou, D., Hatzidimitriou, P., Panagiotopoulos, D., Makropoulos, K., Papadimitriou, P. & Deschamps, A., 1999. Microseismicity and focal mechanisms at the western termination of the North Anatolian Fault and their implications for continental tectonics, *Geophys. J. Int.,* **137,** 891–908.

International Seismological Centre, 2019. *ISC-GEM Earthquake Catalogue*. doi.org /10.31905/d808b825.

Jenny, S., Goes, S., Giardini, D. & Kahle, H.-G., 2004. Earthquake recurrence parameters from seismic and geodetic strain rates in the eastern Mediterranean, *Geophys. J. Int.,* **157,** 1331–1347.

Kagan, Y.Y. & Jackson, D.D., 1991. Long-term earthquake clustering, *Geophys. J. Int.,* **104,** 117–133.

Kahveci, M., Cirmik, A., Dogru, F., Pamukcu, O & Gonenc, T., 2019. Subdividing the tectonic elements of Aegean and Eastern Mediterranean with gravity and GPS data, *Acta Geophys*., **67,** 491–500.

Kiratzi, A.A., Wagner, G. & Langston, C., 1991. Source parameters of some large earthquakes in Northern Aegean determined by body waveform modelling, *Pure appl. Geophys.,* **135,** 515–527.

Kourouklas, C., Papadimitriou, E., Tsaklidis, G & Karakostas, V., 2016. Statistics of earthquake recurrence time in North Aegean Trough, *Bull. Geol. Soc. Greece,* **50**(3), 1349–1358.

Kourouklas, C., Papadimitriou, E., Tsaklidis, G. & Karakostas, V., 2018. Earthquake recurrence models and occurrence probabilities of strong earthquakes in the North Aegean Trough (Greece), *J. Seismol.,* **22,** 1225–1246.

Kreemer, C., Chamot-Rooke, N. & Le Pichon, X., 2004. Constraints on the evolution and vertical coherency of deformation in northern Aegean from a comparison of geodetic, geologic and seismological data, *Earth planet. Sci. Lett.,* **225**(3-4), 329–346.

Le Pichon, X., Lyberis, N. & Alvarez, F., 1987. Discussion on the subsidence of the North Aegean Trough: an alternative view, *J. Geol. Soc,* **144**(2), 349–351.

Leptokaropoulos, K., Papadimitriou, E.E., Orlecka-Sikora, B. & Karakostas, V.G., 2012. Seismicity rate changes in association with the evolution of stress field in northern Aegean Sea, Greece, *Geophys. J.Int.,* **188,** 1322–1338.

Mangira, O., Kourouklas, C., Chorozoglou, D., Iliopoulos, A. & Papadimitriou, E., 2019. Modeling the earthquake occurrence with time-dependent processes: a brief review, *Acta Geophys*., **67,** 739–752.

Mangira, O., Console, R., Papadimitriou, E., Murru, M. & Karakosta, V., 2020. The short-term seismicity of the Central Ionian Islands (Greece) studied by means of a clustering model, *Geophys. J. Int.,* **220,** 856–875.

Mann, H.B & Whitney, D.R., 1947. On a test of whether one of two random variables is stochastically larger than the other, *Ann. Math. Stat.,* **18**(1), 50–60.

Matthews, M. V., Ellsworth, W. L. & Reasenberg, P. A., 2002. A Brownian model for recurrent earthquakes, *Bull. seism. Soc. Am.,* **92**(6), 2233–2250.

McClusky, S. *et al.* 2000. Global positioning system constraints on plate kinematics and dynamics in the eastern Mediterranean and Caucasus, *J. geophys. Res.,* **105,** 5695–5719.

McNeil, L.C., Mille, A., Minshull, T.A., Bull, J.M. & Kenyon, N.H., 2004. Extension of the North Anatolian Fault into the North Aegean Trough: evidence for transtension, strain partitioning, and analogues for the Sea of Marmara basin model, *Tectonics,* **23,** TC2016. doi:10.1029/2002TC001490.

Milne, W. G. & Davenport, A. G., 1969. Earthquake risk in Canada, *Bull. seism. Soc. Am.,* **59,** 49–71.

Muller, M.D., Geiger, A., Kahle, H.-G., Veis, G., Billiris, H., Paradissis, D & Felekis, S., 2013. Velocity and deformation fields in the North Aegean

domain, Greece, and implications for fault kinematics, derived from GPS data 1993–2009, *Tectonophysics,* **597–598,** 34–49.
Nomura, S., Ogata, Y., Komaki, F & Toda, S., 2011. Bayesian forecasting of recurrent earthquakes and predictive performance for a small sample size, *J. geophys. Res.,* **116,** B04315. doi:10.1029/2010JB9007917.
Ogata, Y., 2002. Slip-size-dependent renewal process and Bayesian inferences for uncertainties, *J. geophys. Res.,* **107**(B11), 2268. doi: 10.1029/2001JB9000668.
Papadimitriou, E.E. & Sykes, L.R., 2001. Evolution of the stress field in the northern Aegean Sea (Greece), *Geophys. J. Int.,* **146,** 747–759.
Papanikolaou, D., Alexandri, M., Nomikou, P. & Ballas, D., 2002. Morphotectonic structure of the western part of the North Aegean Basin based on swath bathymetry, *Mar. Geol.,* **190,** 465–492. doi:10.1016/S0025-3227(02)00359-6.
Papanikolaou, D., Alexandri, M. & Nomikou, P., 2006. Active faulting in the north Aegean basin, *Geol. Soc. Am., Space Paper,* **409,** 189–209.
Papazachos, B.C. & Papazachou, C.C., 2000. *The Earthquakes of Greece,* Ziti Publications, 304pp.
Papazachos, B.C., Kiratzi, A.A. & Karacostas, B.G., 1997a. Towards a homogeneous moment-magnitude determination for earthquakes in Greece and the surrounding area, *Bull. seism. Soc. Am.,* **87,** 474–483.
Papazachos, B. C., Karakaisis, G. F., Papadimitriou, E. E. & Papaioannou, Ch. A., 1997b. The regional time and magnitude predictable model and its application to the Alpine-Himalayan belt. *Tectonophysics,* **271,** 295–323.
Papazachos, B.C., Papadimitriou, E.E., Kiratzi, A.A., Papazachos, C.B. & Louvari, E.K., 1998. Fault plane solutions in the Aegean Sea and the surrounding area and their tectonic implications, *Boll. Geofil. Teor. Appl.,* **39,** 199–218.
Papazachos, B. C., Scordilis, M. E., Panagiotopoulos, D. G., Papazachos, C. B. & Karakaisis, G. F., 2004. Global relations between seismic fault parameters and moment magnitude of earthquakes, *Bull. Geol. Soc. Greece,* **36**(3), 1482–1489.
Parsons, T., Geist, E.L., Console, R. & Carluccio, R., 2018. Characteristic earthquake magnitude frequency distribution on faults calculated from consensus data in California, *J. geophys. Res.,* **123**. doi:10.1029/2018JB016539.
Reid, H.F., 1911. The elastic-rebound theory of earthquakes, *Univ. Calif. Pub. Bull. Dept. Geol. Sci.,* **6,** 413–444.
Rhoades, D., Dissen, R. V., Langridge, R., Little, T., Ninis, D., Smith, E. & Robinson, R.(2011). Re-evaluation of conditional probability of rupture of the Wellington-Hutt valley segment of the Wellington fault, *Bull. New Zeal. Soc. Earthq. Eng.,* **44**(2), 77–86.
Rice, J.R., 1992. Fault stress states, pore pressure distributions, and the weakness of the San Andreas fault, in *Fault Mechanics and Transport Properties of Rocks; A Festschrift in Honour of W. F. Brace,* pp. 475–503, eds Evans, B. & Wong, T., Academic Press.
Richards-Dinger, K. & Dieterich, J.H., 2012. RSQSim earthquake simulator, *Seismol. Res. Lett.,* **83,** 983–990.
Robinson, R. & Benites, R., 1996. Synthetic seismicity models for the Wellington Region, New Zealand: Implications for the temporal distribution of large events, *Geophys. Res. Lett.,* **101**(B12), 27,833–27,844.
Robinson, R., Van Dissen, R. & Litchfield, N., 2011. Using synthetic seismicity to evalute seismic hazard in the Wellington region, New Zealand, Geophys, *Geophys. J. Int.,* **187,** 510–528.
Rundle, J.B., 1988. A physical model for earthquakes. 2. Application to southern California, *J. geophys. Res.,* **93,** 6255–6274.
Sachs, M.K., Yikilmaz, M.B., Heien, E.M., Rundle, J.B., Turcotte, D.L. & Kellogg, L.H., 2012. Virtual California earthquake simulator, *Seismol. Res. Lett.,* **83,** 973–978.
Sakellariou, D. *et al.* 2016. Deformation pattern in the western North Aegean Trough: preliminary Results, *Bull. Geol. Soc. Greece,* **50**(1), 124–133. doi:10.12681/bgsg.11708.
Scholz, C.H., 2002. *The Mechanics of Earthquake And Faulting,* 2nd edn, Cambridge Univ. Press, 504pp.
Scholz, C.H., 2010. Large earthquake triggering, clustering and the synchronization of faults, *Bull. seism. Soc. Am.,* **100,** 901–909.
Schultz, K.W., Yoder, M.R., Wilson, J.M., Heien, E.M., Sachs, M.K., Rundle, J.B. & Turcotte, D.L., 2017. Parametrizing physics-based earthquake simulations, *Pure appl. Geophys.,* **174,** 2269–2278. doi:10.1007/s00024-016-1428-3.
Schwartz, D.P., 2018. Past and future rupture lengths in seismic source characterization – the long and short of it, *Bull. seism. Soc. Am.,* **108,** 2493–2520. doi:10.1785/0120160110.
Schwartz, D.P. & Coppersmith, K.J., 1984. Fault behavior and characteristic earthquakes: examples from Wasatch and San Andreas fault zones, *J. geophys. Res.,* **89,** 5681–5698.
Stein, R.S., Barka, A.A. & Dieterich, J.H., 1997. Progressive failure on the North Anatolian Fault since 1939 by earthquake stress triggering, *Geophys. J. Int.,* **128,** 594–604.
Stephens, M.A., 1974. EDF Statistics for Goodness of Fit and some comparisons, *J. Am. Statist. Assoc.,* **64**(374), 730–737. doi:10.2307/2286009.
Taymaz, T., Jackson, J. & McKenzie, D., 1991. Active tectonics of the North and central Aegean Sea, *Geophys. J. Int.,* **106,** 433–490.
Toda, S. & Stein, R.S., 2003. Toggling of seismicity by the 1997 Kagoshima earthquake couplet: a demonstration of time-dependent stress transfer, *J. geophys. Res.,* **108**(B12), 2567. doi:10.1019/2003JB002527.
Toda, S., Stein, R.S., Reasenberg, P.A. & Dieterich, J.H., 1998. Stress transfer by the 1995 *Mw*= 6.9 Kobe, Japan, shock: effect on aftershocks and future earthquake probabilities, *J. geophys. Res.,* **103**(B10), 24, 543-24,565.
Tullis, T.E., 2012. Preface to the focused issue on earthquake simulators, *Seismol. Res. Lett.,* **83,** 957–958.
Valentini, A, Pace, B., Boncio, P., Visini, F., Pagliaroli, A & Pergalani, F., 2019. Definition of seismic input from fault-based PSHA: remarks after the 2016 Central Italy earthquake sequence, *Tectonics,* **38**. doi:10.1029/2018TC005086.
Ward, S.N., 2000. San Francisco Bay area earthquake simulators: a step toward a standard physical earthquake model, *Bull. Seismol. Soc. Am.,* **90,** 370–386.
Ward, S.N., 2012. ALLCALL earthquake simulator, *Seismol. Res. Lett.,* **83,** 964–972.
Weichert, D. H., 1980. Estimation of the earthquake recurrence parameters for unequal observation periods for different magnitudes, *Bull. seism. Soc. Am.,* **70,** 1337–1346.
Wells, D. L. & Coppersmith, K. J., 1994. New empirical relationships among magnitude, rupture length, rupture width, rupture area, and surface displacement, *Bull. seism. Soc. Am.,* **84,** 974–1002.
Wessel, P., Smith, W. H. F., Scharroo, R., Luis, J. & Wobbe, F., 2013. Generic Mapping Tools: improved Version Released, *EOS, Trans. Am. geophys. Un.,* **94,** 409–410.
Wiemer, S. & Wyss, M., 2000. Minimum magnitude of completeness in earthquake catalogs: examples from Alaska, the western United States, and Japan, *Bull. seism. Soc. Am.,* **90,** 859–869. doi:10.1785/0119990114.
Wilcoxon, F., 1945. Individual comparison by ranking methods, *Biometrics,* **1** *(6)*, 80–83.
Yaltirak, C. & Alpar, B., 2002. Kinematics and evolution of the northern branch of the North Anatolian Fault (Ganos Fault) between the Sea of Marmara and the Gulf of Saros, *Mar. Geol.,* **190,** 351–366.
Yang, G., Tang, Y., Lei, D., Hu, Q. & Wu, J., 2020. Holocene activity and seismic hazard analysis of faults in Damxung, Tibet, *Acta Geophys.,* **68,** 597–604.
Yikilmaz, M.B., Turcotte, D.L., Yakovlev, G., Rundle, J.B. & Kellog, L.H., 2010. Virtual California earthquake simulations: simple models and their application to an observed sequence of earthquakes, *Geophys. J. Int.,* **180,** 734–742.

APPENDIX A: STATISTICAL TESTS

A1. Statistical Tests for the best performing simulated catalogue

The evaluation of the best performing simulated catalogue is made by means of two non-parametric hypothesis tests, namely the two sample Kolmogorov–Smirnov (K–S) and the Wilcoxon Rank–Sum.

The two sample K–S test is a non-parametric goodness of fit test, which compares the differences between the empirical cumulative

distribution functions (ecdf), $F(x)$ and $G(x)$, of two samples under the null hypothesis that both originate from the same distribution against the alternative hypothesis that they come from different ones at a given significance level, α. The statistic of the test is defined as:

$$D = \max\left(|F(x) - G(x)|\right). \tag{A1.1}$$

The decision of rejecting or not the null hypothesis is based on the p-value returned by the test, compared with the significance level. If p-value is greater than α (p-value $> \alpha$) then the null hypothesis can not be rejected. On the contrary, if p-value is lower than α (p-value $< \alpha$) the null hypothesis can be rejected.

The Wilcoxon Rank–Sum test compares two independent random variables F and G with sample sizes m and n, respectively, under the null hypothesis that the two samples come from the same distribution, similarly with the Mann–Whitney U-test. The samples are combined and ranked. The Wilcoxon statistic, T, is calculated from the sum of the ranks according to:

$$T_F = \sum_{i=1}^{m} R_{F_i} \tag{A1.2}$$

and

$$T_G = \sum_{j=1}^{n} R_{G_j}. \tag{A1.3}$$

The number of times that $F_i > G_j$ in an ordered arrangement, so called the Mann–Whitney statistic U, is then defined as:

$$U = \min\left(U_F, U_G\right) \tag{A1.4}$$

where

$$U_F = mn + \frac{m(m+1)}{2} - T_F \tag{A1.5}$$

and

$$U_G = mn + \frac{n(n+1)}{2} - T_G. \tag{A1.6}$$

The null hypothesis cannot be rejected if the p-value is larger than the level of significance, α (p-value $\geq \alpha$).

A2. Statistical tests for the recurrence model selection

The comparison between the Poisson and the Renewal (expressed by the BPT distribution) models is made by the application of the Akaike Information Criterion (AIC), along with the non parametric goodness of fit Anderson–Darling test (AD test).

The selection among the candidate models via the AIC is implemented by the calculation and the comparison of its values. The model that displays the best performance is the one with the minimum value of the criterion.

The values of AIC can be calculated by:

$$AIC = -2lnL + 2k \tag{A2.1}$$

where lnL and k stands for the value of the log-likelihood function and the number of parameters of the candidate model, respectively.

The AD test is implemented by calculating the distance, A^2, between the empirical cumulative distribution function (ecdf) and the cumulative distribution function (cdf) for the distributions applied to the data, where

$$A^2 = -n - \sum_{i=1}^{n} \frac{2i-1}{n} \left[lnF(x_i) + \ln\left(1 - F(x_{n+1-1})\right)\right], \tag{A2.2}$$

and $\{x_1, x_2, \ldots, x_n\}$ are the ordered sample data points, n is the number of observations and F is the cdf of the distribution under study. The test compares the factor A^2 with a critical value, c, under the null hypothesis that the data are distributed according to F. If the factor A^2 is less than or equal to the critical value, then the null hypothesis cannot be rejected.